JOURNAL OF GEOPHYSICAL RESEARCH, VOL. 108, NO. B4, 2214, doi:10.1029/2001JB000903, 2003

Transient elastic *P* and *SV* wave edge diffraction by a semi-infinite perfect-slip fracture in an isotropic dispersive solid: A canonical problem

Adrianus T. de Hoop[1] and Maarten V. de Hoop
Center for Wave Phenomena, Colorado School of Mines, Golden, Colorado, USA

Received 16 July 2001; revised 28 October 2002; accepted 23 January 2003; published 23 April 2003.

[1] The canonical problem of edge diffraction of transient *P* or *SV* waves by a perfect-slip (fluid-filled) fracture is investigated. Closed-form analytic expressions for the time domain particle velocities of the reflected, transmitted, and converted waves on either side of the fracture, for the cylindrical edge-diffracted waves, and for the excited Rayleigh surface waves along the plane of the fracture are obtained. The hosting solid is taken to be homogeneous, isotropic, and dispersive. As to the seismic loss mechanism, two cases are considered: the frictional force/bulk viscosity mechanism and the standard linear solid or Zener mechanism. Numerical illustrations of the different wave constituents are presented, including those applying to postcritical incidence of *SV* waves. They deal with the case of a well-developed, stationary fracture; the significance of the results to the theory of fracture mechanics with a view to the problem of a transient load at a crack face is briefly indicated. *INDEX TERMS:* 5112 Physical Properties of Rocks: Microstructure; 5144 Physical Properties of Rocks: Wave attenuation; 7260 Seismology: Theory and modeling; 3210 Mathematical Geophysics: Modeling; *KEYWORDS:* wave attenuation, cracks, edge diffraction

Citation: de Hoop, A. T., and M. V. de Hoop, Transient elastic *P* and *SV* wave edge diffraction by a semi-infinite perfect-slip fracture in an isotropic dispersive solid: A canonical problem, *J. Geophys. Res.*, *108*(B4), 2214, doi:10.1029/2001JB000903, 2003.

1. Introduction

[2] In analyzing the phenomenology of elastic wave propagation in fractured rock one of the methodologies consists of trying to understand the wave properties as the outcome of the multiple scattering by a (large) number of individual fractures. In such considerations the scattering properties of a single fracture, or rather the diffraction properties of each individual edge of it, serve as building blocks in the further analysis, and for the theory to be successful the knowledge of these properties in a manageable, preferably analytic, form is an indispensable prerequisite [see, e.g., *Sih and Loeber*, 1969]. As far as elastic wave scattering is concerned even the simplest configuration of a planar fracture of bounded extent, present in an otherwise homogeneous, isotropic host material, gives already rise to the formation of a number of scattered wave constituents. First of all, an incident wave of the *P*- or *S*-type (with the *S* wave decomposed into an *SH* wave with particle velocity parallel to the edge of the fracture and an *SV* wave with particle velocity in the plane perpendicular to the edge of the fracture) hitting the plane of the fracture gives rise to partially reflected and partially transmitted waves, converted waves, and surface waves. Furthermore, each edge of the fracture gives rise to diffracted waves. Multiple interactions with this degree of complexity can in practice only be handled via computational methods and/or methods of statistical physics, organized about the canonical problem of the scattering by a constituting individual fracture.

[3] A canonical problem of this kind also underlies other applications in geophysics. For example, in wave field imaging and inversion the availability of analytic expressions for the scattered wave constituents enables one to carry out a sensitivity analysis as to design of a data acquisition setup as well as a feasibility study with regard to the performance of the imaging or inversion algorithm employed. For example, a (volumetric) Born imaging inversion will poorly detect a (nonvolumetric) crack-like flaw as opposed to a Kirchhoff imaging inversion procedure [*Kitahara and Nakahata*, 2003]). Furthermore, for cases of such complexity that numerical techniques are the only approach, canonical configurations serve as a benchmark for the accuracy and the possible limitations of the discretization procedures used. Still another type of application where a canonical configuration acts as a useful tool is the carrying out of controlled laboratory experiments. In fact, our study was started in direct relationship to such a case, where hydraulic fracture growth in a piece of rock was monitored while irradiating the fracture with an ultrasonic wave and measuring the scattered wave field. Here, the model data for a known fracture were used to calibrate the wave field transmitted by the transducer. (For an associated field experiment, see *Aki and Fehler* [1982].) In a more theoretical

[1]Permanently at Laboratory of Electromagnetic Research, Faculty of Information Technology and Systems, Delft University of Technology, Delft, Netherlands.

0148-0227/03/2001JB000903$09.00

setting analytically known expressions for scattered wave constituents form the basis for the incorporation of the relevant edge diffraction coefficients in the ray asymptotic treatment of elastic wave scattering [*Achenbach et al.*, 1982].

[4] The canonical problem addressed in this paper is the diffraction of plane, transient, *P* or *SV* waves by a semi-infinite, planar, perfect-slip fracture in a homogeneous, isotropic solid (for a related problem, see *Gu et al.* [1996]). The incident wave models the teleseismic body wave originating far from the edge of the fracture. The perfect-slip condition at the faces of the fracture models the case of fluid-filled fracture (which could be a (microscopic) part of a fault zone). An additional feature that we take into account is seismic loss in the solid host material. First, the edge diffraction problem in a lossless medium is solved with the aid of the combination of the modified Cagniard method for analyzing the transient wave motion in layered media and the Wiener-Hopf or ''factorization'' method that has previously been used to solve the corresponding problems for a semi-infinite rigid baffle and a semi-infinite traction-free (void) crack. In the analysis the complex slowness plane representation of the scattered waves plays a crucial role. The importance of this representation lies in the circumstance that each physical scattered wave constituent is associated with a particular singularity (pole, branch point) in this plane. Next, the influence of losses in the solid is taken into account by applying a ''correspondence theorem'' [*Chao and Achenbach*, 1964; *De Hoop*, 1995b] that relates the wave motion in the lossless case to the one in a medium with a particular loss mechanism via the use of the Schouten-Van der Pol theorem of the time Laplace transformation. The cases that we consider are: the Frictional force/bulk viscosity loss mechanism and the standard linear solid (Zener) creep relaxation loss mechanism [*Carcione*, 2001; *Mainardi*, 2002]. The latter has also been extensively used in seismology [*Liu et al.*, 1976]. Both mechanisms define a causal reaction between stress and strain and therefore satisfy, in the frequency domain, automatically the Kramers-Kronig causality relations, while yielding the associated frequency domain dispersion and attenuation properties of the wave motion involved. Thus we follow the approach of using effective macroscopic relaxation functions without specifying the micromechanical phenomena that cause the attenuation. (For a correlation between velocity dispersion in saturated porous rocks and viscous interaction between solid and fluid phases, see *Winkler* [1985, 1986].)

[5] For the two-dimensional problem under consideration the elastic wave motion decomposes into an *SH* wave with particle velocity parallel to the edge of the fracture and a combined *P-SV* wave with particle velocity in the plane perpendicular to the edge of the fracture. The *SH* case leads to a simple scalar problem and is not reconsidered here. (In fact, it is mathematically the same as for the traction-free fracture.) Only the change in pulse shape due to the presence of either of the two loss mechanisms is reported for this case. The *P-SV* case is considered in detail, both for the lossless case and for either of the two loss mechanisms. Prior to solving the diffraction problem, a spatial symmetry analysis is carried out where the total wave motion is decomposed into an ''odd'' and an ''even'' part (with respect to the plane of the fracture). Such an analysis shows how the solution to the fluid-filled fracture problem is related to (part of) the one for the void fracture. The results for the fluid-filled fracture differ, however, fundamentally from the ones for the traction-free case and are therefore fully discussed, one of the major differences being that the traction-free fracture admits no elastodynamic power flow across the plane of the fracture, while the fluid-filled fracture partially reflects and partially transmits elastodynamic energy.

[6] Studies in the literature on scattering and diffraction by fluid-filled fractures, numerical as well as analytical ones (including those of a ray asymptotic nature) mostly concern themselves with time harmonic waves [*Fehler and Aki*, 1978; *Achenbach et al.*, 1978; *Visscher*, 1981; *Coutant*, 1989]. For experimental results, see, for example, *Pyrak-Nolte et al.* [1990]. The present analysis directly addresses the time domain wave motion.

[7] Transient plane *P* wave diffraction by a void crack of finite width has been studied by *Thau and Lu* [1971] through an iteration scheme of successive edge diffraction interactions. Up to two *P* wave transits across the crack width, they show to be manageable with the combined (iterative) Wiener-Hopf technique and the modified Cagniard method. In the corresponding finite time window they determine the dynamic stress intensity factors.

[8] Although we restrict our considerations to the diffraction by a well-developed, stationary, fracture, the methodology is also directly applicable to the theory of transient loading at a crack face. For this type of application the expressions for the stress components are needed. These admit representations of the same type as the ones for the particle velocity that we do employ. How the relevant correspondence is made is discussed in detail by *Freund* [1998]. A related application is the crack tip propagation (at an assumed constant speed) in an already cracked brittle material induced by a normally incident plane P wave (see *Achenbach and Nuismer*, [1971] and *Freund* [1998, chapter 6] for the relevant theory and *Ravichandran and Clifton* [1989] for experiments in this respect).

2. Formulation of the Problem

[9] Position in three-dimensional configuration space $\mathbb{R}^3$ is specified by the coordinates $\{x_1, x_2, x_3\}$ with respect to an orthogonal Cartesian reference frame with the origin $\mathcal{O}$ and the three mutually perpendicular base vectors $\{\mathbf{i}_1, \mathbf{i}_2, \mathbf{i}_3\}$ of unit length each. The subscript notation for Cartesian vectors and tensors is used and the summation convention applies. Latin subscripts are used for this purpose; they run through the values 1, 2, 3. Wherever appropriate $\mathbf{x}$ denotes vectorial position. The time coordinate is t. Partial differentiation with respect to x_m is denoted by ∂_m; ∂_t is a reserved symbol for differentiation with respect to time. Time convolution is indicated by $\overset{t}{*}$.

[10] The fracture occupies the domain $\Sigma = \{(x_1, x_2, x_3) \mid 0 < x_1 < \infty, -\infty < x_2 < \infty, x_3 = 0\}$ (see Figure 1). The hosting solid is homogeneous and isotropic with volume density of mass ρ, compliance

$$S_{ijpq} = \Lambda\delta_{ij}\delta_{pq} + 2M\Delta_{ijpq}, \quad \Lambda = -\frac{\lambda}{(3\lambda + 2\mu)\,2\mu}, \quad M = \frac{1}{4\mu}, \tag{1}$$

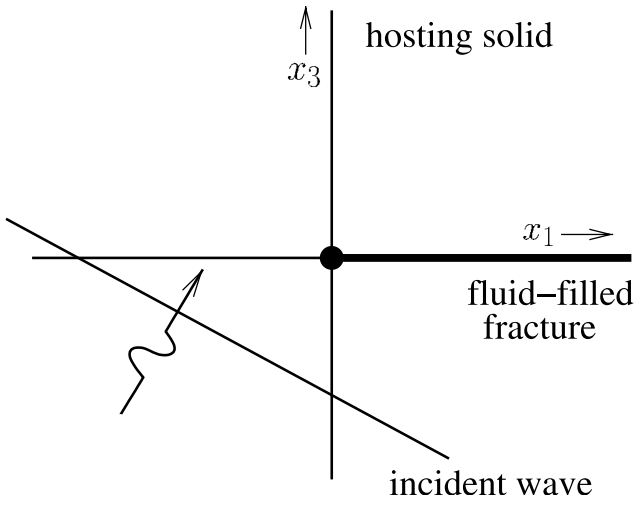

Figure 1. The configuration.

global inertia relaxation function $\phi = \phi(t)$, global compliance relaxation function $\psi = \psi(t)$, where λ and μ are the Lamé coefficients, and

$$\Delta_{ijpq} = \frac{1}{2}\left(\delta_{ip}\delta_{jq} + \delta_{iq}\delta_{jp}\right) \tag{2}$$

is the symmetrical unit tensor of rank four, and δ_{ij} is the Kronecker tensor. The relaxation functions satisfy the causality condition $\phi(t) = 0$ for $t < 0$ and $\psi(t) = 0$ for $t < 0$. For a perfectly elastic (i.e., instantaneously reacting) solid, $\phi(t) = \delta(t)$ and $\psi(t) = \delta(t)$.

2.1. Elastic Wave Motion in the Configuration

[11] In the interior of the solid, the particle velocity $v_r = v_r(\mathbf{x}, t)$ and the dynamic stress $\tau_{pq} = \tau_{pq}(\mathbf{x}, t)$ satisfy the first-order coupled elastic wave equations

$$-\Delta_{kmpq}\partial_m\tau_{pq} + \rho\partial_t\left(\phi \overset{t}{*} v_k\right) = f_k, \tag{3}$$

$$\Delta_{ijnr}\partial_n v_r - S_{ijpq}\partial_t\left(\psi \overset{t}{*} \tau_{pq}\right) = h_{ij}, \tag{4}$$

where $f_k = f_k(\mathbf{x}, t)$ is the volume source density of force and $h_{ij} = h_{ij}(\mathbf{x}, t)$ is the volume source density of deformation rate.

2.2. Boundary Conditions

[12] The fluid-filled fracture is assumed to be stationary. Its action is modeled by the perfect-slip boundary conditions

$$\lim_{x_3\downarrow 0}\{\tau_{13}, \tau_{23}\} = 0, \quad \lim_{x_3\uparrow 0}\{\tau_{13}, \tau_{23}\} = 0 \ \text{ on } \Sigma, \tag{5}$$

$$\lim_{x_3\downarrow 0}\tau_{33} = \lim_{x_3\uparrow 0}\tau_{33}, \quad \lim_{x_3\downarrow 0} v_3 = \lim_{x_3\uparrow 0} v_3 \text{ on } \Sigma, \tag{6}$$

i.e., on either face of the fracture the tangential components of the dynamic traction vanish, while the normal component of the dynamic traction and the normal component of the particle velocity are continuous across the fracture. (In the case of a void fracture all components of the dynamic traction vanish on both faces, while all components of the particle velocity do jump.)

2.3. Excitation

[13] The configuration is excited by an incident plane *P* or *SV* wave, propagating in the $\{x_1, x_3\}$ plane perpendicular to the edge of the fracture. Its particle velocity component parallel to the edge of the fracture vanishes. Its wave field components are indicated by the superscript i. The incident wave is assumed to hit the edge of the fracture at $t = 0$ and has the signature $q^{P,S}(t)$ for *P* and *SV* waves, respectively; $q^{P,S}(t) = 0$ for $t < 0$.

[14] The total wave motion is the superposition of the incident wave and the scattered wave whose components are indicated by the superscript s. Because of the uniformity of the medium as well as the fracture in the x_2 direction, and the isotropy of the solid, the wave diffraction problem is then two-dimensional in nature and independent of x_2. As a consequence, the *SH* wave is decoupled from the *P-SV* waves.

2.4. Symmetry Considerations

[15] Upon decomposing the wave field into an even and an odd part with respect to the symmetry plane $\{x_3 = 0\}$ and invoking the explicit boundary conditions at the fracture together with the continuity conditions across it, it follows from the relevant reflection symmetry considerations that the scattered wave field has a vanishing even part, whence only an odd constituent remains [*De Hoop*, 1995a]. Using Greek subscripts, taking on the values {1, 2}, to denote vector and tensor components in the plane parallel to the fracture this implies that

$$\left\{v^s_\beta, v^s_3\right\}(x_1, x_2, x_3, t) = \left\{-v^s_\beta, v^s_3\right\}(x_1, x_2, -x_3, t), \tag{7}$$

$$\left\{\tau^s_{\gamma\delta}, \tau^s_{\gamma 3}, \tau^s_{3\delta}, \tau^s_{33}\right\}(x_1, x_2, x_3, t) = \left\{-\tau^s_{\gamma\delta}, \tau^s_{\gamma 3}, \tau^s_{3\delta}, -\tau^s_{33}\right\}(x_1, x_2, -x_3, t). \tag{8}$$

These relations are right from the beginning used in the representations for the wave field components.

2.5. Associated Problems in Dynamic Fracture Mechanics

[16] The symmetry considerations also offer a direct clue to the interrelation between the edge diffraction problem under consideration and the uniform transient load crack face separation problem in dynamic fracture mechanics for mode II type of crack opening deformation (in the terminology of *Freund* [1998]). In this type of opening deformation the generated stress-velocity field satisfies the same symmetry conditions as our scattered wave, while its tensile stress loading condition yields a boundary condition that is, up to a minus sign, identical to the one applying to τ^s_{13} for normal incidence. Furthermore, for the case of a suddenly applied (uniform) load, the magnitude of this load is to be derived from our case of plane wave incidence by extracting the load from the corresponding dynamic stress in the plane of the fracture. To facilitate the identification, we shall for

the moment use the terminology of dynamic fracture mechanics, where the tensile and shear stress denote the normal and tangential components of the dynamic stress, respectively.

[17] In the required case of normal incidence only the *SV* wave yields the necessary load. Let its stress field be $\tau^{\mathrm{i}}H(t)$ parallel to the wave front. The corresponding particle velocity signature is then $q(t) = -(\mu\rho)^{-1/2}\tau^{\mathrm{i}}H(t)$. Then, in the notation of equation (10) in section 3, the incident wave will induce on the plane $x_3 = 0$ a shear stress of magnitude $\tau^* = \tau^{\mathrm{i}}$, while the tensile stress vanishes. The relevant boundary conditions are [*Freund*, 1998, equation (2.6.3)]

$$\lim_{x_3\downarrow 0}\tau_{33} = 0,\ -\infty < x_1 < \infty,\ -\infty < x_2 < \infty,$$
$$\lim_{x_3\downarrow 0}\tau_{13} = -\tau^* H(t),\ \text{on } \Sigma,$$
$$\lim_{x_3\downarrow 0} v_1 = 0,\ -\infty < x_1 < 0,\ -\infty < x_2 < \infty.$$

For mode I type of crack opening deformation, the corresponding boundary value problem with even symmetry needs to be solved. The relevant solution can be extracted from the traction-free (void) fracture edge diffraction problem with incident *P* wave at normal incidence [*Freund*, 1998, section 2.4]. The corresponding stress intensity factors follow from using equation (2.1.1) of *Freund* [1998] and substituting in this relation the values of our τ^{s}_{ij} that arise from applying the constitutive relations to the calculated v^{s}_r.

3. Incident Wave Field

[18] Part of the subsequent analysis differs for the two cases of an incident *P* wave and an incident *SV* wave. Let for the lossless case the incident *P* wave be specified by

$$v^{\mathrm{i};P}_{1,3} = c_P\{p_0^P, \gamma_P(p_0^P)\}q^P[t - p_0^P x_1 - \gamma_P(p_0^P)x_3], \tag{9}$$

with $0 \le p_0^P \le c_P^{-1}$ in view of the condition of causality of the scattered wave, $\gamma_P(p_0^P) = (c_P^{-2} - (p_0^P)^2)^{1/2}$ and wave speed $c_P = [(\lambda + 2\mu)/\rho]^{1/2}$. Let the incident *SV* wave be specified by

$$v^{\mathrm{i};SV}_{1,3} = c_S\{-\gamma_S(p_0^S), p_0^S\}q^S[t - p_0^S x_1 - \gamma_S(p_0^S)x_3], \tag{10}$$

with $0 \le p_0^S \le {c_S}^{-1}$ in view of the condition of causality of the scattered wave, $\gamma_S(p_0^S) = (c_S^{-2} - (p_0^S)^2)^{1/2}$ and wave speed $c_S = (\mu/\rho)^{1/2}$. In the range $0 \le p_0^S \le c_P^{-1}$ this amounts to precritical incidence, in the range ${c_P}^{-1} \le p_0^S \le c_S^{-1}$ this amounts to postcritical incidence.

4. Complex Slowness Representations for the Scattered Wave Field Constituents

[19] As assumed, the incident plane wave hits the edge of the fracture at the instant $t = 0$. Then the scattered wave field vanishes for $t < 0$ and its time Laplace transformation is

$$\left\{\hat{v}^{\mathrm{s}}_r, \hat{\tau}^{\mathrm{s}}_{pq}\right\}(\mathbf{x}, s) = \int_0^\infty \exp(-st)\left\{v^{\mathrm{s}}_r, \tau^{\mathrm{s}}_{pq}\right\}(\mathbf{x}, t)\mathrm{d}t, \tag{11}$$

where s is taken to be real and positive. Next, the complex slowness representations pertinent to the lossless case are introduced via

$$\left\{\hat{v}^{\mathrm{s}}_r, \hat{\tau}^{\mathrm{s}}_{pq}\right\}(x_1, x_3, s) = \frac{1}{2\pi\mathrm{i}}\int_{\mathcal{L}} \exp(-spx_1)\left\{\tilde{v}^{\mathrm{s}}_r, \tilde{\tau}^{\mathrm{s}}_{pq}\right\}(p, x_3, s)\,\mathrm{d}p, \tag{12}$$

where i is the imaginary unit and p is the complex slowness parameter in the x_1 direction. The (infinite) path of integration $\mathcal{L}$ in the complex p plane remains to be determined, but a necessary condition for the convergence of the integral is that $\mathcal{L}$ should be parallel to the imaginary p axis as $|p| \to \infty$. The domain to the left of $\mathcal{L}$ will be denoted by $\mathcal{D}^-$, the domain to the right of $\mathcal{L}$ will be denoted by $\mathcal{D}^+$.

[20] Taking into account that the *P* waves in the solid are curl-free and travel in the lossless case with the wave speed c_P, while the *SV* waves are divergence-free and travel in the lossless case with the wave speed c_S and incorporating the symmetry properties of the particle velocity components expressed by equation (7), it is found that the complex slowness domain particle velocities of the scattered *P* and *SV* waves are of the form

$$\tilde{v}^{\mathrm{s};P}_{1,3} = \hat{q}^{P,S}(s)\{\mp p, \gamma_P(p)\}p\gamma_S(p)\tilde{A}^{P,S}(p) \cdot \exp(-s\gamma_P(p)|x_3|), \quad x_3 \lessgtr 0, \tag{13}$$

and

$$\tilde{v}^{\mathrm{s};SV}_{1,3} = \hat{q}^{P,S}(s)\{\pm\gamma_S(p), p\}\left(p^2 - \frac{1}{2}c_S^{-2}\right)\tilde{A}^{P,S}(p) \cdot \exp(-s\gamma_S(p)|x_3|), \quad x_3 \lessgtr 0. \tag{14}$$

Here, it has been taken into account that they travel away from the fracture. The corresponding vertical wave slownesses are

$$\gamma_{P,S} = \left(c_{P,S}^{-2} - p^2\right)^{1/2}, \quad \mathrm{Re}\left(\gamma_{P,S}(p)\right) \ge 0 \text{ for all } p \in \mathbb{C} \tag{15}$$

The total scattered wave consists of the superposition of the scattered *P* and *SV* wave constituents, i.e., $\tilde{v}^{\mathrm{s}}_{1,3} = \tilde{v}^{\mathrm{s};P}_{1,3} + \tilde{v}^{\mathrm{s};SV}_{1,3}$. The corresponding dynamic stresses follow from equations (1) and (4) as

$$s\hat{\tau}^{\mathrm{s}}_{13} = \mu\left(\partial_1\hat{v}^{\mathrm{s}}_3 + \partial_3\hat{v}^{\mathrm{s}}_1\right), \tag{16}$$

$$s\hat{\tau}^{\mathrm{s}}_{33} = \lambda\left(\partial_1\hat{v}^{\mathrm{s}}_1 + \partial_3\hat{v}^{\mathrm{s}}_3\right) + 2\mu\partial_3\hat{v}^{\mathrm{s}}_3. \tag{17}$$

The complex slowness amplitudes $\tilde{A}^{P,S} = \tilde{A}^{P,S}(p)$ referring to *P* and *SV* wave incidence, remain to be determined.

5. Determination of the Scattered *P*/*SV* Wave Complex Slowness Amplitudes

[21] Invoking the condition (6) that $\hat{v}^{\mathrm{s}}_3$ should be continuous across the nonfractured part of the plane $x_3 = 0$, we obtain the relation

$$\frac{1}{2\pi\mathrm{i}}\int_{\mathcal{L}} \gamma_S(p)\tilde{A}^{P,S}(p)\exp(-spx_1)\mathrm{d}p = 0, \qquad -\infty < x_1 < 0. \tag{18}$$

From the explicit boundary condition (5), with the use of equation (16), we furthermore obtain the relation

$$\frac{1}{2\pi\mathrm{i}}\int_{\mathcal{L}}\Delta_R(p)\tilde{A}^{P,S}(p)\exp(-spx_1)\mathrm{d}p=-B^{P,S}\exp\left(-sp_0^{P,S}x_1\right),\qquad 0<x_1<\infty, \tag{19}$$

in which

$$\Delta_R(p)=p^2\gamma_P(p)\gamma_S(p)+\left(p^2-\frac{1}{2}c_S^{-2}\right)^2 \tag{20}$$

is the Rayleigh determinant whose zeros are $p=\pm c_R^{-1}$, where c_R is the wave speed of Rayleigh surface waves along a traction-free boundary of a semi-infinite perfectly elastic solid, and

$$B^P=c_Pp_0^P\gamma_P\left(p_0^P\right), \tag{21}$$

$$B^S=c_S\left[\left(p_0^S\right)^2-\frac{1}{2}c_S^{-2}\right] \tag{22}$$

for incident P and SV, respectively. Equations (18), (19) constitute a standard Wiener-Hopf problem.

[22] The Wiener-Hopf problem to be solved is of the generic form

$$\frac{1}{2\pi\mathrm{i}}\int_{\mathcal{L}}\gamma_S(p)\tilde{A}(p)\exp(-spx_1)\mathrm{d}p=0,\qquad -\infty<x_1<0, \tag{23}$$

$$\frac{1}{2\pi\mathrm{i}}\int_{\mathcal{L}}\Delta_R(p)\tilde{A}(p)\exp(-spx_1)\mathrm{d}p=-B\exp(-sp_0x_1),\qquad 0<x_1<\infty. \tag{24}$$

Equation (23) is satisfied if

$$\gamma_S(p)\tilde{A}(p)=F^-(p),\qquad p\in\mathcal{L}\cup\mathcal{D}^-, \tag{25}$$

where $F^-=F^-(p)$ is some function that is regular in $\mathcal{D}^-$ and has the property $F^-(p)=o(1)$ as $|p|\to\infty$ in $\mathcal{D}^-$, uniformly in $\arg(p)$. The proof follows by applying Cauchy's theorem and Jordan's lemma to $\mathcal{L}\cup\mathcal{D}^-$.

[23] Equation (24) is satisfied if

$$\Delta_R(p)\tilde{A}(p)=\frac{B}{p-p_0}+H^+(p),\qquad p\in\mathcal{L}\cup\mathcal{D}^+, \tag{26}$$

where $H^+=H^+(p)$ is some function that is regular in $\mathcal{D}^+$ and has the property $H^+(p)=o(1)$ as $|p|\to\infty$ in $\mathcal{D}^+$, uniformly in $\arg(p)$, provided that $\mathcal{L}$ is chosen such that $p_0\in\mathcal{D}^+$. The proof follows by applying the residue theorem and Jordan's lemma to $\mathcal{L}\cup\mathcal{D}^+$. Combining equations (25) and (26), we arrive at

$$\frac{\Delta_R(p)}{\gamma_S(p)}F^-(p)=\frac{B}{p-p_0}+H^+(p),\qquad p\in\mathcal{L}. \tag{27}$$

Equation (27) belongs to the class of Wiener-Hopf relations [*Wiener and Hopf*, 1931; *Titchmarsh*, 1948; *Baker and Copson*, 1950; *Noble*, 1958; *Achenbach*, 1973; *Freund*, 1998] and is amenable to a solution with the aid of the factorization method [*Weinstein*, 1969]. (Note that in our approach equation (27) is only required to hold on a line and not in a strip of nonvanishing width as usually claimed in the literature.)

[24] The crucial step in the further solution to the problem is to "factorize" the functions multiplying $\tilde{A}(p)$ into a factor (with superscript minus) that is regular in $\mathcal{D}^-$ and a factor (with superscript plus) that is regular in $\mathcal{D}^+$. For $\gamma_S(p)$ such a factorization is obtained by inspection as

$$\gamma_S(p)=\gamma_S^-(p)\gamma_S^+(p),\qquad p\in\mathcal{L}, \tag{28}$$

where

$$\gamma_S^\mp(p)=\left(c_S^{-1}\mp p\right)^{1/2}\quad\text{with }\mathrm{Re}\left(\gamma_S^\mp\right)\geq 0 \tag{29}$$

is regular in $\mathcal{D}^\mp$.

[25] For $\Delta_R(p)$ the factorization requires the application of the Plemelj formulas [*Noble*, 1958; *Sparenberg*, 1958]. For this purpose we rewrite $\Delta_R(p)$ as

$$\Delta_R(p)=\frac{c_S^{-2}-c_P^{-2}}{2}\left(c_R^{-2}-p^2\right)K(p),\qquad p\in\mathcal{L}. \tag{30}$$

To show that $\log K(p)$ meets the conditions for Plemelj decomposition, we observe that a Taylor expansion around $p=\infty$ yields $K(p)=1+O(p^{-2})$ as $|p|\to\infty$ along $\mathcal{L}$. Furthermore, as equation (30) shows, $K(p)$ can be continued analytically away from $\mathcal{L}$ into the entire p plane cut along the common branch cuts of $\gamma_P(p)\gamma_S(p)$, i.e., along $\{p\in\mathbb{C};\ c_P^{-1}<|\mathrm{Re}(p)|<c_S^{-1},\ \mathrm{Im}(p)=0\}$. Additive Plemelj decomposition of $\log K(p)$ leads upon exponentiation to

$$K(p)=K^-(p)K^+(p),\qquad p\in\mathcal{L}, \tag{31}$$

where $K^-(p)$ as given by equations (A8) and (A12) is regular in $\mathcal{D}^-$ and $K^+(p)$ as given by equations (A8) and (A13) is regular in $\mathcal{D}^+$. Note that $\gamma_S^-(p)=\gamma_S^+(-p)$ and $K^-(p)=K^+(-p)$.

[26] With the aid of equations (28)–(31), equation (27) is cast into the form

$$\left(\frac{c_S^{-2}-c_P^{-2}}{2}\right)\left(\frac{1}{c_R}-p\right)\frac{K^-(p)}{\gamma_S^-(p)}F^-(p)-B\frac{\gamma_S^+(p_0)}{K^+(p_0)}\frac{1}{c_R^{-1}+p_0}\frac{1}{p-p_0}$$
$$=B\left[\frac{\gamma_S^+(p)}{K^+(p)}\frac{1}{c_R^{-1}+p}-\frac{\gamma_S^+(p_0)}{K^+(p_0)}\frac{1}{c_R^{-1}+p_0}\right]\frac{1}{p-p_0}$$
$$+\frac{\gamma_S^+(p)}{K^+(p)}\frac{1}{c_R^{-1}+p}H^+(p),\quad p\in\mathcal{L}. \tag{32}$$

By taking $\mathcal{L}$ such that the branch points $p=c_P^{-1}$ and $p=c_S^{-1}$ of $K^-(p)$, the branch point $p=c_S^{-1}$ of $\gamma_S^-(p)$ as well as the simple pole $p=c_R^{-1}$ of $(c_R^{-1}-p)^{-1}$ and the simple pole $p=p_0$ of $(p-p_0)^{-1}$ are all located in $\mathcal{D}^+$ and the branch points $p=-c_P^{-1}$ and $p=-c_S^{-1}$ of $K^+(p)$, the branch point $p=-c_S^{-1}$

of $\gamma_S^+(p)$ as well as the simple pole $p = -c_R^{-1}$ of $(c_R^{-1} + p)^{-1}$ are all located in $\mathcal{D}^-$, the left-hand side of this equation is regular in $\mathcal{D}^-$ and the right-hand side is regular in $\mathcal{D}^+$. According to Liouville's first theorem [*Titchmarsh*, 1950, p. 85], the left-hand side and the right-hand side of equation (32) are then representations of one and the same entire function that is regular in the entire p plane. Since the left-hand side is of order $o(p^{1/2})$ as $|p| \to \infty$ in $\mathcal{D}^-$ and the right-hand side is of order $o(p^{-1/2})$ as $|p| \to \infty$ in $\mathcal{D}^+$, this entire function is, by virtue of Liouville's second theorem [*Titchmarsh*, 1950, p. 85], identically equal to zero. Consequently, by putting the left-hand side equal to zero, we obtain an expression for $F^-(p)$ which with equation (25) leads to

$$\tilde{A} = B\frac{2}{c_S^{-2} - c_P^{-2}}\frac{\gamma_S^-(p)}{\gamma_S(p)K^-(p)(c_R^{-1} - p)}\frac{\gamma_S^+(p_0)}{K^+(p_0)}\frac{1}{c_R^{-1} + p_0} \cdot \frac{1}{p - p_0}, \quad p \in \mathcal{L}. \tag{33}$$

Using this result in equations (13)–(14) yields the complex slowness amplitudes of the scattered particle velocities.

[27] To arrive at the space-time expressions for the particle velocities of the scattered P and SV waves, the analytic continuation of $\tilde{A}$ into the entire complex p plane is needed. To this end, the definitions of $\gamma_S^{\mp}$ and $K^{\mp}$ are taken to hold in the entire cut p plane.

6. Time Domain Expressions for the Scattered Waves

[28] The final step in the analysis consists of extracting from the now known complex slowness representations of the particle velocities of the scattered wave constituents their time domain counterparts. Writing $\hat{v}_{1,3}^{s;P,SV}$ as $\hat{q}^{P,S}\hat{G}_{1,3}^{s;P,SV}$, the generic form of $\hat{G}_{1,3}^{s;P,SV}$ is

$$\hat{G}_{1,3}^{s;P,SV} = \frac{1}{2\pi i}\int_{\mathcal{L}} \tilde{g}_{1,3}^{s;P,SV} \exp\{-s[px_1 + \gamma_{P,S}(p)|x_3|]\}\mathrm{d}p, \tag{34}$$

in which s only occurs in the exponential function. Once $G_{1,3}^{s;P,SV} = G_{1,3}^{s;P,SV}(x_1, x_3, t)$ has been determined, we have

$$v_{1,3}^{s;P,SV} = q^{P,S}(t) \overset{t}{*} G_{1,3}^{s;P,SV}(x_1, x_3, t). \tag{35}$$

To determine $G_{1,3}^{s;P,SV}$ the modified Cagniard method is used. Accordingly, the path of integration $\mathcal{L}$ in the complex p plane is replaced with the one along which (modified Cagniard path)

$$px_1 + \gamma_{P,S}(p)|x_3| = \tau, \tag{36}$$

where τ is taken to be real and positive, and plays the role of time parameter. In the process of contour deformation, no branch cuts (that make $\gamma_{P,S}^{\mp}$ and $K^{\mp}$ single-valued) may be crossed, while passing either one of the poles $p = p_0^{P,S}$ or $p = 1/c_R$ (note that $p = -1/c_R$ is on account of equation (33) not a pole of $\tilde{g}_{1,3}^{s;P,SV}$) must each time be accounted for by incorporating the corresponding residue.

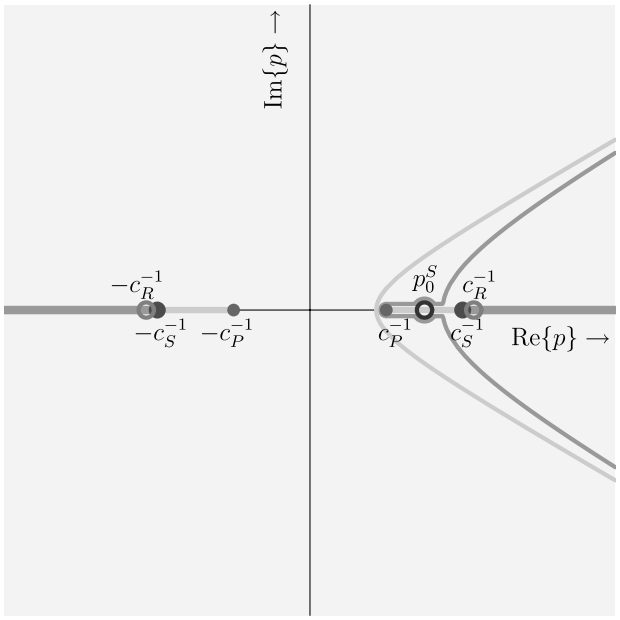

Figure 2. Modified Cagniard contours (postcritical *SV* incidence).

[29] Solving equation (36) for p leads to the P and S hyperbolic body wave paths $\{p \in \mathbb{C}; p = p_{P,S}\} \cup \{p \in \mathrm{C}; p = p_{P,S}^*\}$, in which the asterisk denotes complex conjugate, where

$$p_{P,S} = p_{P,S}(x_1, |x_3|, \tau) = \frac{x_1}{r^2}\tau + i\frac{|x_3|}{r^2}\left(\tau^2 - T_{P,S}^2\right)^{1/2}, \quad T_{P,S} < \tau < \infty, \tag{37}$$

in which $r = (x_1^2 + x_3^2)^{1/2}$ is the distance from the edge of the fracture to the point of observation and

$$T_{P,S} = r/c_{P,S} \tag{38}$$

is the P, S wave travel time from the edge of the fracture to the point of observation. Furthermore, the prohibition of the S wave path to cross the P wave branch cut leads to the head wave loop $\{p \in \mathbb{C}; p = p_H\} \cup \{p \in \mathrm{C}; p = p_H^*\}$ around that branch cut, with

$$p_H = p_H(x_1, |x_3|, \tau) = \frac{x_1}{r^2}\tau - \frac{|x_3|}{r^2}\left(T_S^2 - \tau^2\right)^{1/2} + i0 \quad x_1/r > c_S/c_P, \quad T_H < \tau < T_S, \tag{39}$$

with

$$T_H = x_1/c_P + \left(c_S^{-2} - c_P^{-2}\right)^{1/2}|x_3| \tag{40}$$

being the travel time of the (shear) head wave from the edge of the fracture to the point of observation. As indicated, the head wave is only present in the wedge-like region $x_1/r > c_S/c_P$. The modified Cagniard paths are shown in Figure 2.

[30] Introducing τ as the variable of integration, we obtain the path contributions (which will lead to the cylindrical edge-diffracted waves)

$$\hat{G}^{\mathrm{d};P,SV}_{1,3} = \frac{1}{\pi}\int_{T_{P,S}}^{\infty} \exp(-s\tau)\mathrm{Im}\left[\tilde{g}^{\mathrm{s};P,SV}_{1,3}(p_{P,S})\frac{\partial p_{P,S}}{\partial \tau}\right]\mathrm{d}\tau, \quad (41)$$

and the loop contribution (which will lead to the edge-diffracted head wave)

$$\hat{G}^{\mathrm{d};H}_{1,3} = \{0,1\}\frac{1}{\pi}\int_{T_H}^{T_S} \exp(-s\tau)\mathrm{Im}\left[\tilde{g}^{\mathrm{s};SV}_{1,3}(p_H)\frac{\partial p_H}{\partial \tau}\right]\mathrm{d}\tau, \quad \{x_1/r < c_S/c_P, x_1/r > c_S/c_P\}. \quad (42)$$

The uniqueness property of the time Laplace transform for real, positive s [*Widder*, 1946] then leads to the time domain expressions

$$G^{\mathrm{d};P,SV}_{1,3} = \frac{1}{\pi}\mathrm{Im}\left[\tilde{g}^{\mathrm{s};P,SV}_{1,3}(p_{P,S})\frac{\partial p_{P,S}}{\partial \tau}\right]H(t-T_{P,S}) \quad (43)$$

for diffracted body wave constituents, and

$$G^{\mathrm{d};H}_{1,3} = \{0,1\}\frac{1}{\pi}\mathrm{Im}\left[\tilde{g}^{\mathrm{s};SV}_{1,3}(p_H)\frac{\partial p_H}{\partial \tau}\right][H(\tau-T_H)-H(\tau-T_S)], \quad \{x_1/r < c_S/c_P, x_1/r > c_S/c_P\}, \quad (44)$$

for diffracted head wave constituents.

[31] The contributions that, during the contour deformation, arise from passing either of the poles $p = p_0^{P,S}$ associated with the incident plane waves are all in accordance with the geometrical theory of diffraction and are therefore denoted as the geometrical parts of the scattered waves. Combining them with the incident waves, they are all of the form

$$\begin{aligned}\hat{G}^{\mathrm{g};P,SV}_{1,3} &= \tilde{g}^{\mathrm{i};P,SV}_{1,3}\left(p_0^{P,S}\right)\exp\left\{-s\left[p_0^{P,S}x_1 + \gamma_{P,S}\left(p_0^{P,S}\right)x_3\right]\right\} \\ &\quad -\left\{0,\frac{1}{2},1\right\}\mathrm{Res}_{p=p_0^{P,S}}\left[\tilde{g}^{\mathrm{s};P,SV}_{1,3}(p)\right] \\ &\quad \cdot\exp\left\{-s\left[p_0^{P,S}x_1+\gamma_P\left(p_0^{P,S}\right)|x_3|\right]\right\}, \\ &\quad \left\{x_1/r < c_{P,S}p_0^{P,S},\ x_1/r = c_{P,S}p_0^{P,S},\ x_1/r > c_{P,S}p_0^{P,S}\right\}.\end{aligned} \quad (45)$$

Their time domain expressions follow as

$$\begin{aligned}G^{\mathrm{g};P,SV}_{1,3} &= \tilde{g}^{\mathrm{i};P,SV}_{1,3}\left(p_0^{P,S}\right)\delta\left[t-p_0^{P,S}x_1-\gamma_{P,S}\left(p_0^{P,S}\right)x_3\right] \\ &\quad -\left\{0,\frac{1}{2},1\right\}\mathrm{Res}_{p=p_0^{P,S}}\left[\tilde{g}^{\mathrm{s};P,SV}_{1,3}(p)\right] \\ &\quad \cdot\delta\left(t-\left[p_0^{P,S}x_1+\gamma_P\left(p_0^{P,S}\right)|x_3|\right]\right), \\ &\quad \left\{x_1/r < c_{P,S}p_0^{P,S},\ x_1/r = c_{P,S}p_0^{P,S}, x_1/r > c_{P,S}p_0^{P,S}\right\},\end{aligned} \quad (46)$$

from which the relevant plane wave reflection and transmission coefficients follow. With the full residue as indicated, the expression for SV wave incidence only holds for precritical incidence ($0 < p_0^S < 1/c_P$). For postcritical incidence ($1/c_P < p_0^S < 1/c_S$) the full residue has to replaced with Re $\{\mathrm{Res}_{p=p_0^S+\mathrm{i}0}[\tilde{g}^{\mathrm{s};P,S}_{1,3}(p)]\}$.

[32] Finally, the pole $p = 1/c_R$ is only for $x_1 \geq 0$, $x_3 = 0$, i.e., for points of observation on the faces of the fracture, located on the modified path of integration. Its contribution yields the Rayleigh surface wave along the fracture.

[33] With this, the framework for the solution in the lossless case has been completed. The details will be listed below.

6.1. Scattered *P* Wave–Incident *P* Wave

[34] For this case, the framework yields the following substitutions:

$$\left\{\tilde{g}^{\mathrm{i};P}_1, \tilde{g}^{\mathrm{i};P}_3\right\} = \left\{c_P p_0^P, c_P\gamma_P\left(p_0^P\right)\right\} \quad (47)$$

for the incident wave, and

$$\left\{\tilde{g}^{\mathrm{s};P}_1, \tilde{g}^{\mathrm{s};P}_3\right\} = \left\{\mp p^2\gamma_S(p), p\gamma_P(p)\gamma_S(p)\right\}\tilde{A}^P(p), \quad x_3 \lessgtr 0, \quad (48)$$

for the scattered wave constituent. The geometrical contribution is obtained from

$$\mathrm{Res}_{p=p_0^P}\left\{\tilde{g}^{\mathrm{s};P}_1(p), \tilde{g}^{\mathrm{s};P}_3(p)\right\} = \left\{\pm\left(p_0^P\right)^2\gamma_S\left(p_0^P\right), -p_0^P\gamma_P\left(p_0^P\right)\gamma_S\left(p_0^P\right)\right\}, \quad R^P\left(p_0^P\right) \quad x_3 \lessgtr 0, \quad (49)$$

in which

$$R^P\left(p_0^P\right) = \mathrm{Res}_{p=p_0^P}\tilde{A}^P(p) = \frac{B^P}{\Delta_R\left(p_0^P\right)}. \quad (50)$$

6.2. Scattered *SV* Wave–Incident *P* Wave

[35] For this case, the framework yields the following substitutions:

$$\left\{\tilde{g}^{\mathrm{s};SV}_1, \tilde{g}^{\mathrm{s};SV}_3\right\} = \left\{\pm\gamma_S(p)\left(p^2-\frac{1}{2}c_S^{-2}\right), p\left(p^2-\frac{1}{2}c_S^{-2}\right)\right\}\tilde{A}^P(p), \quad x_3 \lessgtr 0, \quad (51)$$

for the scattered wave constituent. The geometrical contribution is obtained from

$$\mathrm{Res}_{p=p_0^P}\left\{\tilde{g}^{\mathrm{s};P}_1(p), \tilde{g}^{\mathrm{s};\mathrm{P}}_3(p)\right\} = \left\{\mp\gamma_S\left(p_0^P\right)\left[\left(p_0^P\right)^2-\frac{1}{2}c_S^{-2}\right], -p_0^P\left[\left(p_0^P\right)^2-\frac{1}{2}c_S^{-2}\right]\right\}R^P\left(p_0^P\right), \quad x_3 \lessgtr 0, \quad (52)$$

in which $R^P(p_0^P)$ is given in equation (50).

6.3. Scattered Wave in the Plane of the Fracture–Incident *P* Wave

[36] In the plane of the fracture, we have $x_3 = 0$ and hence the P and SV wave Cagniard paths coincide, with the consequence that the two contributions can be taken together. This procedure is necessitated in the process of contour deformation from $\mathcal{L}$ to the present Cagniard path,

$$\left\{p = \frac{\tau}{x_1} + \mathrm{i}0\right\} \cup \left\{p = \frac{\tau}{x_1} - \mathrm{i}0\right\}, \quad |x_1|/c_P < \tau < \infty, \tag{53}$$

in order that Jordan's lemma applies. The P plus SV combination yields, using equations (13)–(14) at $x_3 = 0$,

$$\left\{\tilde{g}_1^{\mathrm{s};P+SV}, \tilde{g}_3^{\mathrm{s};P+SV}\right\}(p, \mp 0, s) = \left\{\mp\frac{1}{2}\gamma_S(p)c_S^{-2}, \left[p\gamma_P(p)\gamma_S(p) + p\left(p^2 - \frac{1}{2}c_S^{-2}\right)\right]\right\}\tilde{A}^P(p). \tag{54}$$

The cases $x_1 < 0$ and $x_1 > 0$ require different treatments and will be discussed separately below.

6.3.1. Unruptured Part

[37] For the unruptured part we have $x_1 < 0$. Observing that $\gamma_S(p)c_S^{-2}\tilde{A}^P(p)$ (compare equation (25)) is free from singularities in $\mathcal{D}^-$, it then follows that

$$\hat{G}_1^{\mathrm{s};P+SV}(x_1, \mp 0, s) = 0, \quad x_1 < 0. \tag{55}$$

Consequently,

$$v_1^{\mathrm{s};P+SV}(x_1, \mp 0, t) = 0, \qquad x_1 < 0, \tag{56}$$

which is in accordance with symmetry property equation (7).

[38] Furthermore, the remaining component consists of a diffracted only:

$$G_3^{\mathrm{d};P+SV} = \frac{1}{\pi x_1}\mathrm{Im}\left[\left[p\gamma_P(p)\gamma_S(p) + p\left(p^2 - \frac{1}{2}c_S^{-2}\right)\right]\cdot\tilde{A}^P(p)\right]\Bigg|_{p=t/x_1+\mathrm{i}0} H(t + x_1/c_P), \qquad x_1 < 0. \tag{57}$$

6.3.2. Ruptured Part

[39] For the ruptured part we have $x_1 > 0$. For this case, we replace $\mathcal{L}$ by the loop (53), thereby passing the pole $p = p_0^P$. Furthermore, the contribution from the pole $p = c_R^{-1}$, which is situated on the loop, has to be taken into account. Via this procedure, the pole contribution from $p = p_0^P$ yields the geometrical part

$$G_1^{\mathrm{g};P+SV}(x_1, \mp 0, t) = \pm\frac{1}{2}c_S^{-2}\gamma_S(p_0^P)R^P(p_0^P)\delta(t - p_0^P x_1), \quad x_1 > 0, \tag{58}$$

$$G_3^{\mathrm{g};P+SV}(x_1, \mp 0, t) = -\left[p_0^P\gamma_P(p_0^P)\gamma_S(p_0^P) + p_0^P\left[(p_0^P)^2 - \frac{1}{2}c_S^{-2}\right]\right]\cdot R^P(p_0^P)\delta(t - p_0^P x_1), \quad x_1 > 0, \tag{59}$$

while the loop contribution yields the diffracted part

$$G_1^{\mathrm{d};P+SV}(x_1, \mp 0, t) = \mp\frac{1}{2\pi x_1 c_S^2}\mathrm{Im}\left[\gamma_S(p)\tilde{A}^P(p)\right]|_{p=t/x_1} \cdot H(t - x_1/c_P), \quad x_1 > 0, \tag{60}$$

where the value $t = x_1/c_R$ has to be approached from either side, and

$$G_3^{\mathrm{d};P+SV}(x_1, \mp 0, t) = \frac{1}{\pi x_1}\mathrm{Im}\left[\left[p\gamma_P(p)\gamma_S(p) + p\left(p^2 - \frac{1}{2}c_S^{-2}\right)\right]\cdot\tilde{A}^P(p)\right]\Bigg|_{p=t/x_1} H(t - x_1/c_P) - \left[c_R^{-1}\gamma_P(c_R^{-1})\,\gamma_S(c_R^{-1}) + c_R^{-1}\left(c_R^{-2} - \frac{1}{2}c_S^{-2}\right)\right] \cdot \mathrm{Res}_{p=c_R^{-1}}\tilde{A}^P(p)\,\delta(t - x_1/c_R), \quad x_1 > 0. \tag{61}$$

In the last result, the first term on the right-hand side yields a nonvanishing contribution in the interval $x_1/c_P < t < x_1/c_S$ only, while the second term represents the isolated contribution from the Rayleigh surface wave.

6.4. Scattered *P* and *SV* Waves–Incident *SV* Wave

[40] The results for the incident SV wave follow from the ones that are given above for the P wave by the replacing p_0^P, B^P, $\tilde{A}^P(p)$ and $R^P(p_0^P)$ by p_0^S, B^S, $\tilde{A}^S(p)$ and $R^S(p_0^S)$, in which

$$R^S(p_0^S) = \mathrm{Res}_{p=p_0^S}\tilde{A}^S(p) = \frac{B^S}{\Delta_R(p_0^S)} \tag{62}$$

for precritical incidence, i.e., $0 \le p_0^S < c_P^{-1}$ (for which case $\gamma_P(p_0^S)$ is real valued) and

$$R^S(p_0^S) = \mathrm{Re}\left[\mathrm{Res}_{p=p_0^S+\mathrm{i}0}\tilde{A}^S(p)\right] = \mathrm{Re}\left[\frac{c_S\left[(p_0^S + \mathrm{i}0)^2 - \frac{1}{2}c_S^{-2}\right]}{\Delta_R(p_0^S + \mathrm{i}0)}\right], \tag{63}$$

for $c_P^{-1} \le p_0^S < c_S^{-1}$ (i.e., for postcritical incidence for which case $\gamma_P(p_0^S + \mathrm{i}0)$ is negative imaginary).

[41] The difference in results for precritical and postcritical incidence arise from the fact that at postcritical incidence the line of intersection of the wave front of the incident wave with the plane of the fracture travels along the fracture with a speed that is less than c_P (though always with a speed greater than or equal to c_S). In that regime, the simple pole that is indicative for the direction of incidence is now located on the branch cut associated with the diffracted P wave. As a consequence, the application of the residue theorem has now to be modified in the sense that two semicircular arcs on either side of the branch cut are introduced to avoid the pole. These semicircular arcs break up symmetrically the loop associated with the head wave contribution. Taking together their contributions, we arrive at equation (63) as the corresponding expression for $R^S(p_0^S)$.

7. Incorporation of Loss Mechanisms in the Hosting Solid

[42] In this section, global relaxation in the solid is included in the analysis. The relevant mechanism is represented through the global relaxation functions $\phi = \phi(t)$ for the inertia and $\psi = \psi(t)$ for the compliance in equations (3)–(4). The consequences of this are most easily investigated in the complex frequency or s domain. In particular, the particle velocity elastodynamic wave equation yields, for the present case, the key to the application of the correspondence principle [*Chao and Achenbach*, 1964; *De Hoop*, 1995b]. At any interior point of the solid, the s domain particle velocity satisfies the source-free differential equation

$$\left(c_P^2 - c_S^2\right)\partial_k\partial_r\hat{v}_r + c_S^2\partial_r\partial_r\hat{v}_k - s^2\hat{\phi}(s)\hat{\psi}(s)\hat{v}_r = 0. \tag{64}$$

Hence the result of the introduction of the relaxation mechanism is to replace s^2 in the elastodynamic wave equation by $s^2\hat{\phi}(s)\hat{\psi}(s)$. Since, further, the boundary conditions at the crack are of the homogeneous type, the spectral representations of the scattered wave field quantities can now profitably taken to be of the form

$$\left\{\hat{v}_r, \hat{\tau}_{pq}\right\}(x_1, x_3, s) = \frac{1}{2\pi\mathrm{i}}\int_{\mathcal{L}} \exp\left\{-s\left[\hat{\phi}(s)\hat{\psi}(s)\right]^{1/2} p x_1\right\} \cdot\left\{\tilde{v}_r, \tilde{\tau}_{pq}\right\}(p, x_3, s)\mathrm{d}p. \tag{65}$$

In this respect, it is of importance to observe that for linear, causal, dissipative solids, $\hat{\phi}(s)$ and $\hat{\psi}(s)$ are real and positive for positive real values of s and bounded away from 0, while $\hat{\phi}(s) = 1 + o(1)$ and $\hat{\psi}(s) = 1 + o(1)$ as $s \to \infty$. Each scattered wave field spectral constituent is of the general shape

$$\tilde{w}(p, x_3, s) = \hat{q}(s)\tilde{g}(p, x_3), \tag{66}$$

with, now,

$$\tilde{g}(p, x_3) = \tilde{A}(p)\exp\left\{-s\left[\hat{\phi}(s)\hat{\psi}(s)\right]^{1/2}\gamma_{P,S}(p)|x_3|\right\}, \tag{67}$$

where $\gamma_{P,S}(p)$ is, still, given by equation (15). The factorization method remains unaltered, whereas the modified Cagniard method now leads to complex frequency domain expressions of the type

$$\hat{g}(p, x_3, s) = \frac{1}{\pi}\int_{T_{P,S}}^{\infty} \exp\left\{-s\left[\hat{\phi}(s)\hat{\psi}(s)\right]^{1/2}\tau\right\}\mathrm{Im}\left[\tilde{A}(p_{P,S})\frac{\partial p_{P,S}}{\partial\tau}\right]\mathrm{d}\tau \tag{68}$$

for diffracted body wave contributions and

$$\hat{g}(x_1, x_3, s) = \frac{1}{\pi}\int_{T_H}^{T_S} \exp\left\{-s\left[\hat{\phi}(s)\hat{\psi}(s)\right]^{1/2}\tau\right\}\mathrm{Im}\left[\tilde{A}(p_H)\frac{\partial p_H}{\partial\tau}\right]\mathrm{d}\tau \tag{69}$$

for diffracted head wave contributions.

[43] Now, for a number of relaxation functions, $\exp\{-s[\hat{\phi}(s)\,\hat{\psi}(s)]^{1/2}\tau\}$ admits a representation of the type

$$\exp\left\{-s\left[\hat{\phi}(s)\hat{\psi}(s)\right]^{1/2}\tau\right\} = \int_{\tau}^{\infty}\exp(-st)U(t,\tau)\mathrm{d}t. \tag{70}$$

Using equation (70) in equation (69), we end up with

$$g(x_1, x_3, t) = \left[\int_{T_{P,S}}^{t} U(t,\tau)G(x_1, x_3, \tau)\mathrm{d}\tau\right]H\left(t - T_{P,S}\right) \tag{71}$$

for diffracted body wave contributions and

$$g(x_1, x_3, t) = \left[\int_{T_H}^{\min(t,T_S)} U(t,\tau)G(x_1, x_3, \tau)\mathrm{d}\tau\right] \cdot[H(t - T_H) - H(t - T_S)], \tag{72}$$

for diffracted head wave contributions. Here, $G(x_1, x_3, \tau)$ is, in all cases, the scattered wave constituent pertaining to the lossless case for which $\phi(t) = \delta(t)$ and $\psi(t) = \delta(t)$. The intervening function $U = U(t, \tau)$ is referred to as the loss influence kernel function. Obviously, $U(t, \tau) = \delta(t - \tau)$ for the lossless case. In most cases of practical interest, $U(t, \tau)$ has to be determined by solving the Laplace transform equation with the aid of the Bromwich inversion integral.

7.1. Special Case: Elastodynamic Creep/Relaxation Loss Mechanism

[44] The building block for the model of attenuation proposed by *Liu et al.* [1976] can be derived from the standard linear solid with creep/relaxation loss mechanism, also known as the Zener solid. The complete model is based upon a spectrum of these relaxation mechanisms, and is well established in global earth seismology; it plays a role for example in investigating the mantle's composition.

[45] The time domain kernel function for the elastodynamic global creep/relaxation loss mechanism will be determined by applying the Bromwich inversion integral to the Laplace transform expression for the kernel function.

7.1.1. Standard Linear Solid With Creep/Relaxation Loss Mechanism

[46] The isotropic "standard linear solid" with a creep/relaxation loss mechanism, or Zener solid, has the global relaxation functions [*Carcione*, 2001; *Mainardi*, 2002]

$$\phi(t) = \delta(t)\,,\psi(t) = \delta(t) + \left(\frac{1}{\tau_\sigma} - \frac{1}{\tau_\epsilon}\right)\exp\left(-\frac{t}{\tau_\epsilon}\right)H(t). \tag{73}$$

Correspondingly,

$$\hat{\phi}(s) = 1\,,\quad \hat{\psi}(s) = 1 + \frac{1/\tau_\sigma - 1/\tau_\epsilon}{1/\tau_\epsilon + s}. \tag{74}$$

In these expressions, τ_σ is the stress relaxation time and τ_ϵ is the strain relaxation time. On account of the physical condition of creep yield, equation (73) leads to the condition

$$\tau_\sigma < \tau_\epsilon. \tag{75}$$

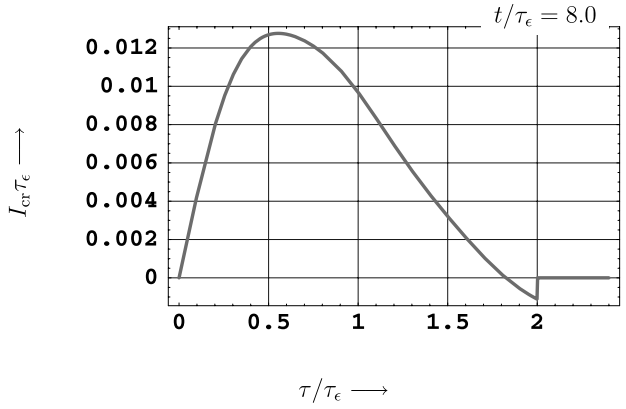

Figure 3. Branch cut contribution to kernel function along t axis.

In the remainder of this section we assume that this condition is satisfied.

7.1.2. Determination of the Loss Influence Kernel Function

[47] The time Laplace transform of the kernel function associated with elastic wave propagation in a solid with losses according to the elastodynamic creep/relaxation function is given by (compare equation (70))

$$\widehat{U}_{\rm cr}(s,\tau) = \exp\left[-s\tau\left(\frac{s+1/\tau_\sigma}{s+1/\tau_\epsilon}\right)^{1/2}\right], \tag{76}$$

in which τ is the time parameter introduced in the modified Cagniard transformation as before. The corresponding time domain function has the Bromwich integral representation

$$U_{\rm cr}(t,\tau) = \frac{1}{2\pi\imath}\int_{s=-\imath\infty}^{\imath\infty} \exp(st)\widehat{U}_{\rm cr}(s,\tau)\mathrm{d}s. \tag{77}$$

Observing that

$$\exp\left[s\tau - s\tau\left(\frac{s+1/\tau_\sigma}{s+1/\tau_\epsilon}\right)^{1/2}\right] = \exp\left[-\frac{1}{2}\left(\frac{1}{\tau_\sigma}-\frac{1}{\tau_\epsilon}\right)\tau\right] \cdot\left[1+O\left(s^{-1}\right)\right] \tag{78}$$

as $|s| \to \infty$, uniformly in arg(s), and noting that

$$\frac{1}{2\pi\imath}\int_{s=-\imath\infty}^{\imath\infty} \exp(st-s\tau)\mathrm{d}s = \delta(t-\tau), \tag{79}$$

where $\delta(t-\tau)$ is the Dirac delta distribution operative at $t=\tau$, application of Jordan's lemma, together with Cauchy's theorem of complex function theory yields

$$U_{\rm cr}(t,\tau) = \exp\left[-\frac{1}{2}\left(\frac{1}{\tau_\sigma}-\frac{1}{\tau_\epsilon}\right)\tau\right]\delta(t-\tau) + \left\{\frac{1}{2\pi\imath}\oint_{C_{\rm cr}} \exp\left[st - s\tau\left(\frac{s+1/\tau_\sigma}{s+1/\tau_\epsilon}\right)^{1/2}\right]\mathrm{d}s\right\}H(t-\tau), \tag{80}$$

where $C_{\rm cr}$ is the loop, in counterclockwise orientation, around the branch cut joining the branch points $s = -1/\tau_\sigma$ and $s = -1/\tau_\epsilon$. This loop integral has to be evaluated numerically. Noting that $(s+1/\tau_\epsilon)^{1/2} = \pm 1(u-1/\tau_\epsilon)^{1/2}$ for $1/\tau_\epsilon < u < 1/\tau_\sigma$ along the upper/lower part $C_{\rm cr}^{\pm}$ of $C_{\rm cr}$ and $(s+1/\tau_\sigma)^{1/2} = (1/\tau_\sigma - u)^{1/2}$ for $1/\tau_\epsilon < u < 1/\tau_\sigma$ along $C_{\rm cr}$, we have

$$I_{\rm cr} = \frac{1}{2\pi\imath}\oint_{C_{\rm cr}} \exp\left[st - s\tau\left(\frac{s+1/\tau_\sigma}{s+1/\tau_\epsilon}\right)^{1/2}\right]\mathrm{d}s = \frac{1}{\pi}\int_{u=1/\tau_\epsilon}^{1/\tau_\sigma} \exp(-ut)\sin\left[u\tau\left(\frac{1/\tau_\sigma-u}{u-1/\tau_\epsilon}\right)^{1/2}\right]\mathrm{d}u \tag{81}$$

To evaluate this expression numerically, we normalize the integration interval from 0 to 1, namely,

$$u = \frac{1}{\tau_\epsilon} + \left(\frac{1}{\tau_\sigma}-\frac{1}{\tau_\epsilon}\right)v, \qquad 0 \le v \le 1. \tag{82}$$

This transformation leads to

$$I_{\rm cr} = \frac{1}{\pi}\left(\frac{1}{\tau_\sigma}-\frac{1}{\tau_\epsilon}\right)\int_{v=0}^{1} \exp\left\{-\left[\frac{1}{\tau_\epsilon}+\left(\frac{1}{\tau_\sigma}-\frac{1}{\tau_\epsilon}\right)v\right]t\right\} \cdot\sin\left\{\left[\frac{1}{\tau_\epsilon}+\left(\frac{1}{\tau_\sigma}-\frac{1}{\tau_\epsilon}\right)v\right]\tau\left(\frac{1-v}{v}\right)^{1/2}\right\}\mathrm{d}v. \tag{83}$$

This integral has an essential singularity at $v = 0$, which has to be handled with proper care. The branch cut contributions $I_{\rm cr}$ are illustrated in Figure 3 for $t/\tau_\epsilon = 8.0$ and Figure 4 for $\tau/\tau_\epsilon = 2.0$.

7.2. Special Case: Frictional Forces and Maxwell-Type Viscoelasticity

[48] The isotropic frictional force Maxwell solid has the global relaxation functions [*Kolsky*, 1964, p. 107]

$$\phi(t) = \delta(t) + \alpha H(t)\,, \quad \psi(t) = \delta(t) + \beta H(t), \tag{84}$$

in which $\alpha > 0$ and $\beta > 0$. Correspondingly,

$$\hat{\phi}(s) = 1 + \frac{\alpha}{s}, \tag{85}$$

$$\hat{\psi}(s) = 1 + \frac{\beta}{s}. \tag{86}$$

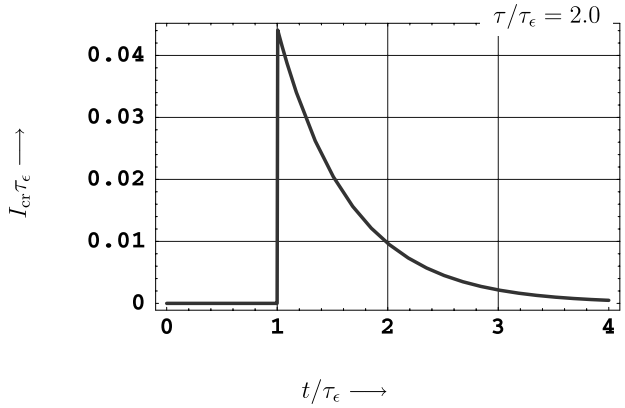

Figure 4. Branch cut contribution to kernel function along τ axis.

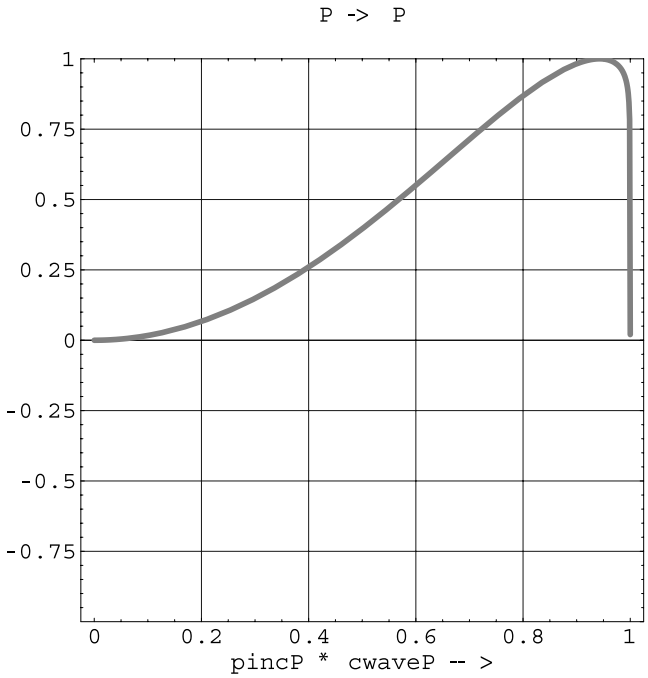

Figure 5. *P*/*P* reflection coefficient (equations (50), (46), and (48)).

For this case, the relation corresponding to equation (70) becomes [*Abramowitz and Stegun*, 1965, formula 29.3.91]

$$\exp\left[-(s+\alpha)^{1/2}(s+\beta)^{1/2}\tau\right] = \int_{\tau}^{\infty} \exp(-st)U_M(t,\tau)\mathrm{d}t, \quad (87)$$

in which

$$U_M(t,\tau) = -\partial_\tau U_0(t,\tau), \quad (88)$$

with

$$U_0(t,\tau) = \exp[-(\alpha+\beta)t/2]I_0\left[(|\beta-\alpha|/2)\left(t^2-\tau^2\right)^{1/2}\right]H(t-\tau), \quad (89)$$

where I_0 denotes the modified Bessel function of the first kind and order 0. Carrying out the differentiation in the right-hand side of equation (88) yields

$$U_M(t,\tau) = \exp[-(\alpha+\beta)t/2]\,\delta(t-\tau) + \exp[-(\alpha+\beta)t/2] \cdot(|\beta-\alpha|/2)\tau\left(t^2-\tau^2\right)^{-1/2}I_1\left[(|\beta-\alpha|/2)\left(t^2-\tau^2\right)^{1/2}\right] \cdot H(t-\tau). \quad (90)$$

8. Discussion of the Results

[49] The earlier sections provide exact time domain expressions for the Green's functions of the different constituents out of which the scattered wave motion is composed in the lossless case. In all of them, the features associated with plane wave diffraction by a semi-infinite fluid-filled fracture show up: geometrically scattered parts of the wave motion, diffracted cylindrical waves, diffracted head waves and Rayleigh surface waves along the fracture. Also, the phenomena associated with postcritical incidence of a plane *SV* wave are quantitatively obtained. Upon convolving the expressions with the signature of the incident plane wave motion, the relevant scattered waves result. Several important features will be extracted from the analytical expressions.

[50] The plane wave reflection coefficients govern the geometrical part of the diffracted waves. These plane wave reflection coefficients do depend on the direction of incidence and they differ for the two types of incident waves and the two types of reflected/transmitted waves. In this respect, it is observed that the boundary conditions (5)–(6) that describe the behavior of the fluid-filled fracture, entail a partial reflection and a partial transmission across the plane of the fracture, a phenomenon that is absent for both a traction-free fracture and for a perfectly rigid baffle.

[51] Figures 5, 6, 7, and 8show the relevant plane wave reflection coefficients as functions of the direction of incidence for the ratio $c_S/c_P = 0.75$. The ones pertaining to *P* wave incidence follow from equation (50); the ones pertaining to *SV* wave incidence follow from equations (62)–(63). For *SV* incidence the reflection coefficients show a marked behavior in the neighborhood of critical direction of incidence. Note that at postcritical incidence no geometrical part to the scattered *P* wave exists.

[52] The analytical expressions in the earlier sections also provide the excitation coefficients of the Rayleigh surface wave along the fracture. In this respect, we observe (see equation (61)) that the component of the particle velocity normal to the plane of the fracture contains an isolated reproduction of the signature of the incident wave starting at the arrival time x_1/c_R of the Rayleigh wave, whereas the

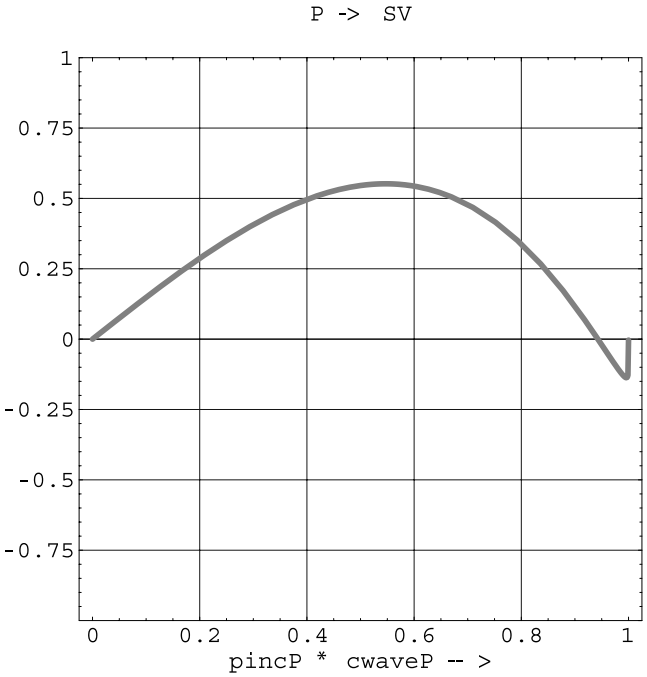

Figure 6. *P*/*SV* reflection coefficient (equations (50), (46), and (51)).

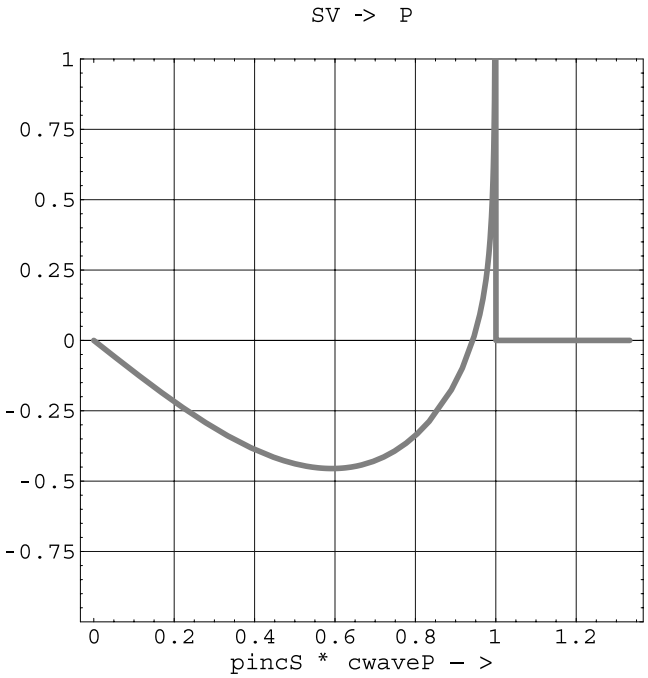

Figure 7. *SV*/*P* reflection coefficient.

Figure 9. *P* incidence Rayleigh excitation coefficient (equation (61)).

component of the particle velocity parallel to the fracture (see equation (60)) shows a time behavior that results upon convolving the signature of the incident wave with the function $(1/c_R - t/x_1)^{-1}$. Figures 9 and 10 present the Rayleigh surface wave excitation coefficients that are defined through the magnitudes of the Rayleigh wave contribution to the component of the particle velocity normal to the plane of the fracture, for incident *P* waves and incident *SV* waves, respectively.

[53] From the expressions for the diffracted parts of the scattered *P* and *SV* waves the "first-motion" cylindrical wave diffraction coefficients that are the key to the geometrical theory of diffraction [*Achenbach et al.*, 1982] by fractures of the type under consideration can be extracted. The relevant diffraction coefficients are geometrical quantities that only depend on the direction of incidence of the plane wave ("incident" geometrical ray) and the direction of observation of the cylindrical diffracted wave ("emerg-

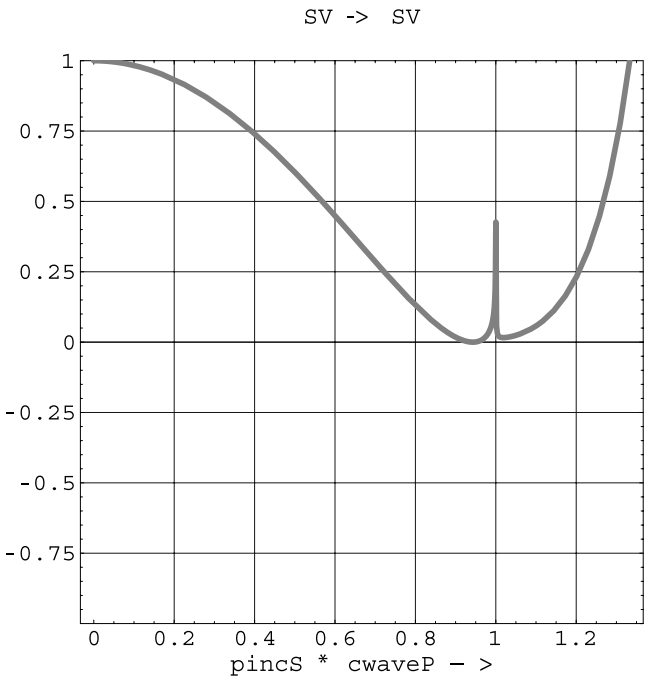

Figure 8. *SV*/*SV* reflection coefficient (from equations (62) and (63)).

Figure 10. *SV* incidence Rayleigh excitation coefficient.

ing" geometrical ray). The first-motion time behavior is normalized to the time behavior of the cylindrical wave emitted by a line source located at the edge of the fracture.

[54] For the case of an incident P wave the first-motion expression for the diffracted P wave is written as

$$v_1^{\mathrm{d};P} \sim \mp\frac{x_1}{r}\, D^{P\to P}\left[q(t) \overset{t}{*} \frac{1}{2\pi\,(t^2 - T_P^2)^{1/2}}\right] H(t - T_P), \quad x_3 \lessgtr 0, \tag{91}$$

$$v_3^{\mathrm{d};P} \sim \frac{|x_3|}{r}\, D^{P\to P}\left[q(t) \overset{t}{*} \frac{1}{2\pi\,(t^2 - T_P^2)^{1/2}}\right] H(t - T_P) \tag{92}$$

and the one for the diffracted SV wave as

$$v_1^{\mathrm{d};S} \sim \pm\frac{|x_3|}{r}\, D^{P\to SV}\left[q(t) \overset{t}{*} \frac{1}{2\pi\,(t^2 - T_S^2)^{1/2}}\right] H(t - T_S), \quad x_3 \lessgtr 0, \tag{93}$$

$$v_3^{\mathrm{d};S} \sim \frac{x_1}{r}\, D^{P\to SV}\left[q(t) \overset{t}{*} \frac{1}{2\pi\,(t^2 - T_S^2)^{1/2}}\right] H(t - T_S), \tag{94}$$

where the factors in front of $D^{P\to P}$ and $D^{P\to SV}$ have been anticipated from the results. Using equation (33) for the complex slowness plane scattering amplitude pertaining to an incident P wave,

$$\frac{\partial p_P}{\partial \tau} = \frac{\mathrm{i}\gamma_P(p_P)}{(\tau^2 - T_P^2)^{1/2}}, \quad \frac{\partial p_S}{\partial \tau} = \frac{\mathrm{i}\gamma_S(p_S)}{(\tau^2 - T_S^2)^{1/2}}, \tag{95}$$

together with equations (35) and (43) for the diffracted P wave and corresponding equations for the diffracted SV wave, the following expressions are obtained:

$$D^{P\to P} = 2\mathrm{Re}\left[c_P^{-1} p_1^P \gamma_S(p_1^P)\tilde{A}^P(p_1^P)\gamma_P(p_1^P)\right], \tag{96}$$

where

$$p_1^P = p_P(x_1, x_3, T_P) = c_P^{-1}(x_1/|x_3|) \tag{97}$$

specifies the direction of observation for the diffracted P wave, and

$$D^{P\to SV} = 2\mathrm{Re}\left[c_S^{-1}\left((p_1^S)^2 - \frac{1}{2}c_S^{-2}\right)\tilde{A}^P(p_1^S)\gamma_S(p_1^S)\right], \tag{98}$$

where

$$p_1^S = p_S(x_1, x_3, T_S) = c_S^{-1}(x_1/|x_3|) \tag{99}$$

specifies the direction of observation for the diffracted SV wave.

[55] For the case of an incident SV wave, the first-motion expressions for the diffracted P and P waves follow from equations (91)–(94) upon replacing by $D^{P\to P}$ by $D^{SV\to P}$ and $D^{P\to SV}$ by $D^{SV\to SV}$. Using the complex slowness plane scattering amplitude pertaining to an incident SV wave, we find

$$D^{SV\to P} = 2\mathrm{Re}\left[c_P^{-1} p_1^P \gamma_S(p_1^P)\tilde{A}^S(p_1^P)\gamma_P(p_1^P)\right] \tag{100}$$

and

$$D^{SV\to SV} = 2\mathrm{Re}\left[c_S^{-1}\left((p_1^S)^2 - \frac{1}{2}c_S^{-2}\right)\tilde{A}^S(p_1^S)\gamma_S(p_1^S)\right]. \tag{101}$$

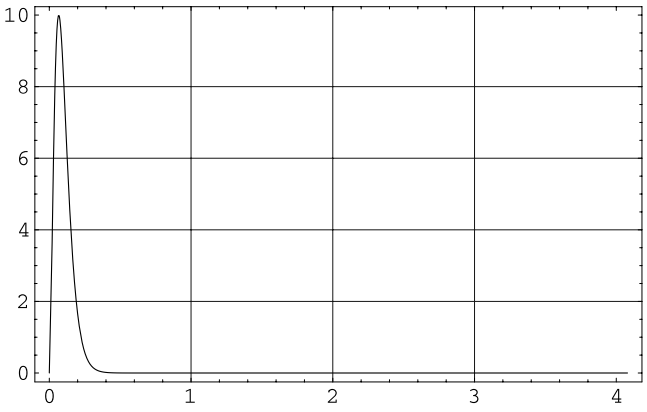

Figure 11. Signature of incident plane wave.

9. Space-Time Elastic Wave Motion: Examples

[56] In this section, first some numerical results as to the total wave motion due to the diffraction of a plane incident P, SV or SH wave by the fluid-filled fracture for the lossless case will be presented. For the case of an incident SV wave both precritical and postcritical incidence will be illustrated. Second, the influence of losses of the creep relaxation and the frictional force Maxwell types on the pulse shapes of the diffracted waves will be illustrated for the case of an SH wave.

9.1. Incident Wave Source Signature

[57] The source signature of the incident plane wave is taken to be the power exponential pulse,

$$q(t) = A\left(\frac{\alpha t}{\nu}\right)^{\nu} \exp(-\alpha t + \nu)\, H(t). \tag{102}$$

Here, A is the amplitude of the pulse (reached at the instant $t = \nu/\alpha$) and the parameters ν and α are related to the pulse risetime t_r and the pulse time width t_w via $\alpha t_r = \nu$, $t_w/t_r = \nu^{-(\nu+1)} \exp(\nu)\, \Gamma(\nu + 1)$. The pulse risetime and the pulse time width must satisfy the condition $t_w > t_r > 0$, with $\nu > 0$ and $\alpha > 0$. The pulse shape is shown in Figure 11.

9.2. Particle Velocity Density Plots in Space at a Given Time

[58] We present density plots of particular components of the particle velocity in space at a given time and some of their constituents (diffracted parts of the scattered wave) as well as for the total wave motion. Since in these plots possible relaxation effects do not manifestly show up, we restrict the density plots to the lossless case.

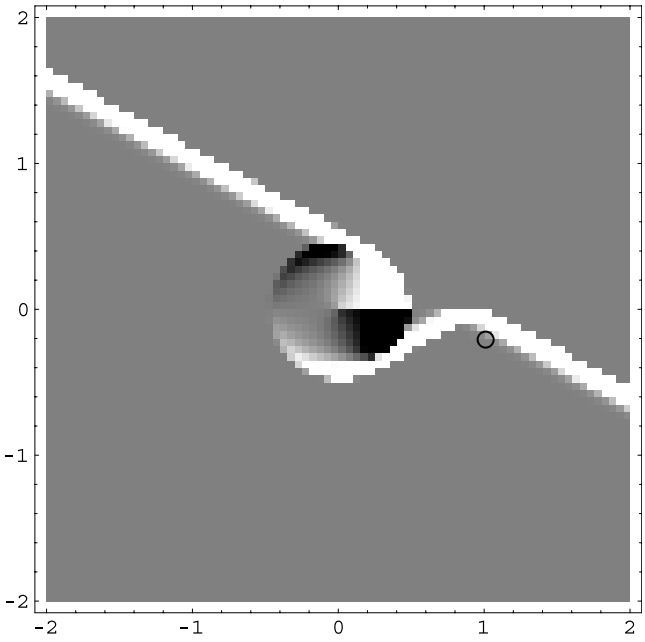

Figure 12. *SH*, snapshot of the total field (v_2).

9.2.1. *SH* Wave Scattering

[59] For comparison, we illustrate the wave field in the case of *SH* wave scattering. The analysis of this case is covered in the literature [*Achenbach*, 1973, section 9.5]. The snapshot for the total field is shown in Figure 12. Note in particular that across the "shadow boundaries" of the geometrically diffracted wave constituent, the total field is continuous. In this case there is no elastodynamic energy transfer across the fracture.

9.2.2. *P*/*SV* Wave Scattering (Incident *P* Wave)

[60] For the particle velocity component parallel to the plane of the fracture, the *P* and *SV* diffraction contributions, as they follow from equations (35) and (43), are shown in Figure 13. The snapshot for the total field is shown in Figure 14. Note in particular that, again, across the shadow boundaries of the geometrically diffracted wave constituents, the total field is continuous.

[61] The particle velocity component normal to the plane of the fracture (Figure 14, right) clearly reveals the Rayleigh wave constituent (more so than the component parallel to the fracture (Figure 14, left)). This is consistent with what has earlier been said about the Rayleigh surface wave excitation coefficient.

9.2.3. *P*/*SV* Wave Scattering (Incident *SV* Wave, Precritical)

[62] For the particle velocity component parallel to the plane of the fracture we show the *P* and *SV* diffraction contributions in Figure 15. The snapshot for the total field is shown in Figure 16. Note in particular that, again, across the shadow boundaries of the geometrically diffracted wave constituents, the total field is continuous.

[63] In the particle velocity component normal to the plane of the fracture (Figure 16, right), the Rayleigh wave constituent clearly shows up (more so than the component parallel to the fracture (Figure 16, left)). This is consistent with what has earlier been said about the Rayleigh surface wave excitation coefficient.

9.2.4. *P*/*SV* Wave Scattering (Incident *SV* Wave, Postcritical)

[64] For the particle velocity component parallel to the plane of the fracture we show the *P* and *SV* diffraction contributions in Figure 17. The snapshot for the total field is shown in Figure 18. Note in particular that, again, across the shadow boundaries of the geometrically diffracted wave constituents, the total field is continuous.

[65] In the particle velocity component normal to the plane of the fracture (Figure 18, right), the Rayleigh wave constituent clearly shows up (more so than in the component parallel to the fracture Figure 18, left) which is

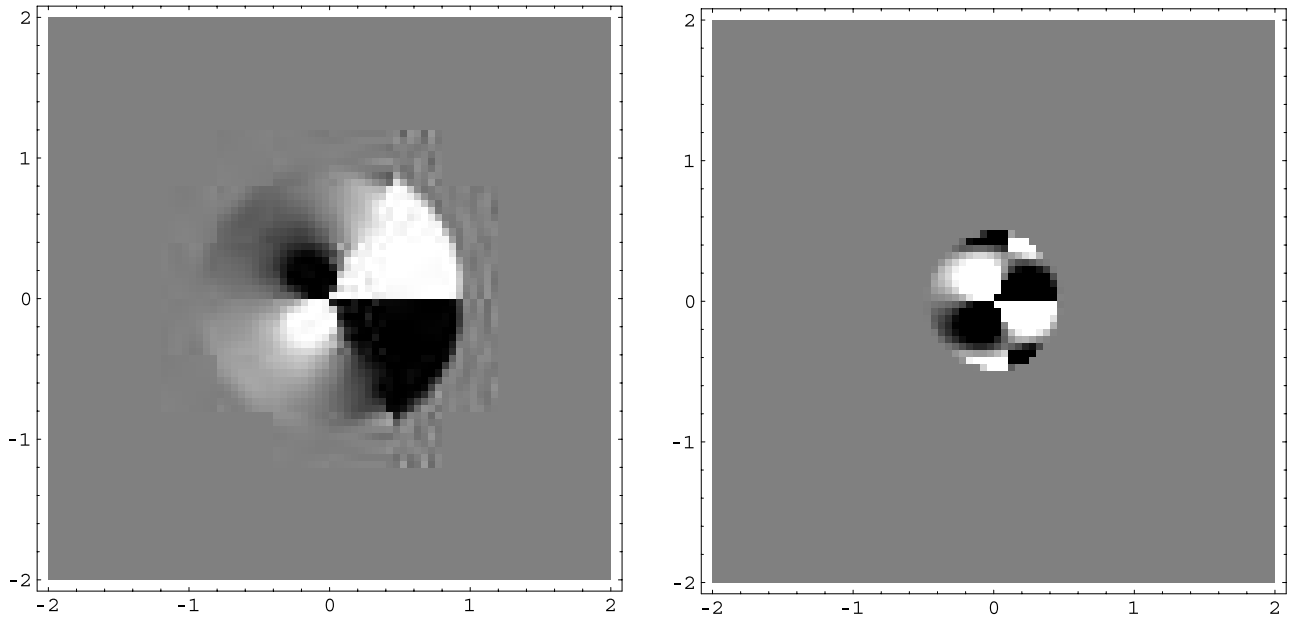

Figure 13. *P*/*SV*, incident *P*, snapshot of (left) the diffracted *P* wave contribution and (right) the diffracted *SV* wave contribution to v_1.

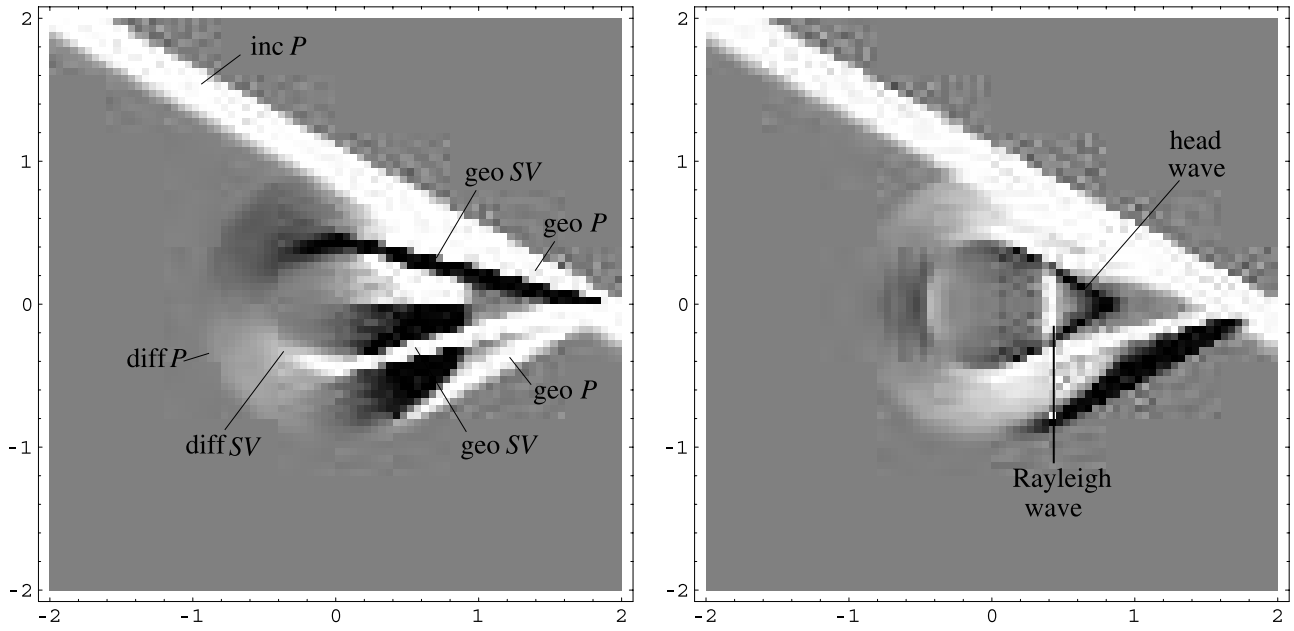

Figure 14. *P*/*SV*, incident *P*, snapshot of (left) v_1 and (right) v_3.

consistent with what has earlier been said about the Rayleigh surface wave excitation coefficient discussed.

[66] In the case of *P*/*SV* wave excitation partial reflection and transmission of elastodynamic energy across the fracture takes place. A particular feature of postcritical *SV* wave incidence is furthermore that there is no geometric (plane) wave contribution to the scattered *P* wave.

9.3. Particle Velocity Time Traces at a Given Position

[67] Effects of pulse amplitude decrease and pulse broadening due to diffraction at the fracture and/or relaxation phenomena in the solid show up much more pronouncedly in a time trace of a particular component of the particle velocity at a given point in space than in a density plot in space at a given time. For this reason we have included some time traces of the *SH* wave particle velocity at a position where the different effects do manifestly show up.

[68] Figure 19 shows a time trace for a perfectly elastic solid. Note that in this case the incident wave and the reflected wave have the same amplitude and the same signature. Figures 20 and 21 show, at the same position,

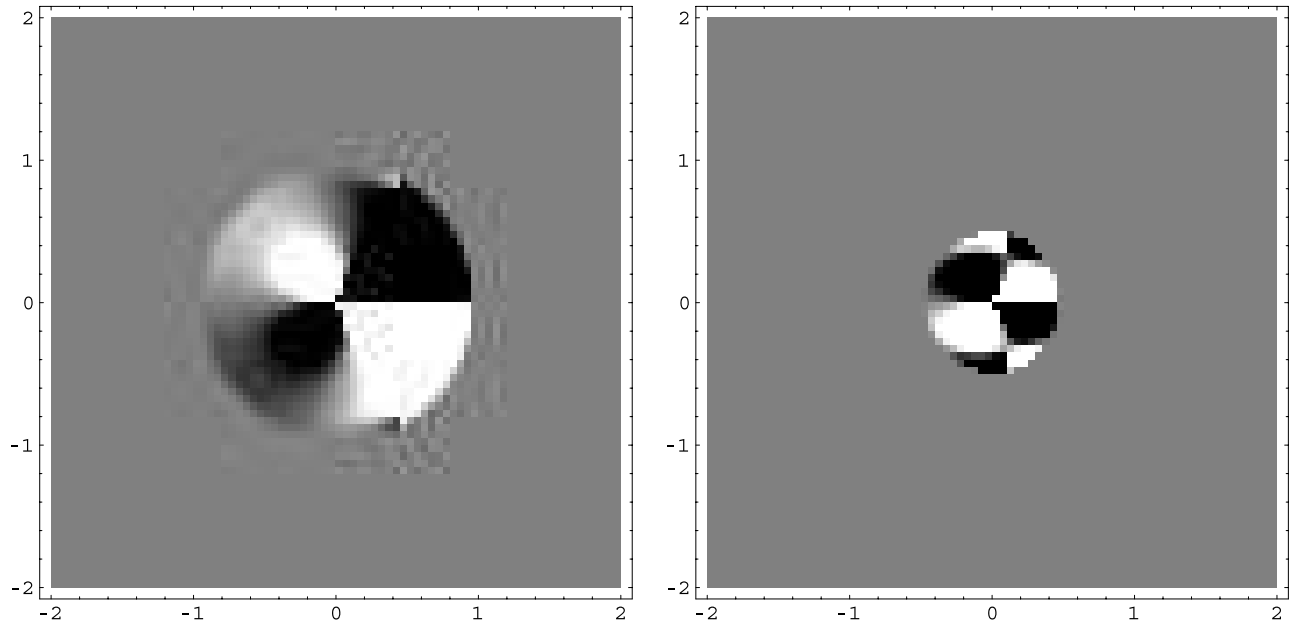

Figure 15. *P*/*SV*, incident *SV*, snapshot of (left) the diffracted *P* wave contribution and (right) the diffracted *SV* wave contribution to v_1; precritical.

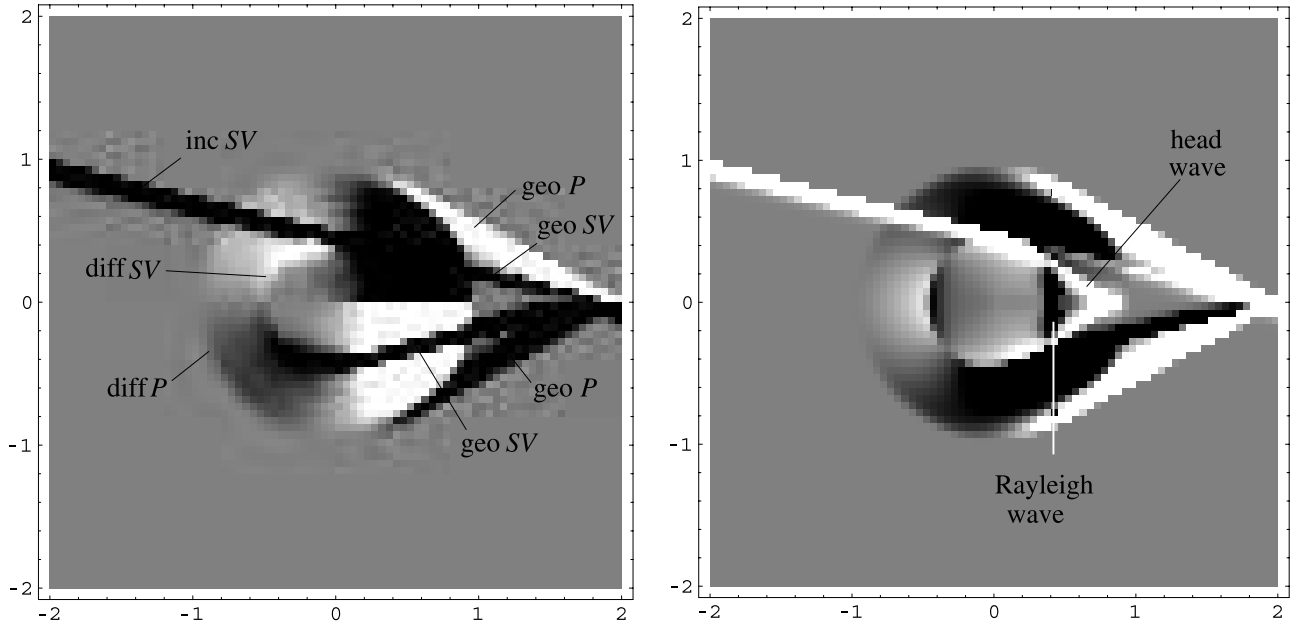

Figure 16. *P*/*SV*, incident *SV*, snapshot of (left) v_1 and(right) v_3; precritical.

time traces for a solid with frictional force Maxwell-type relaxation coefficients $\alpha = 0.2$ and $\beta = 0.1$. Figure 20 shows the relaxation effect due to the first term in the right-hand side of equation (90). This term yields an attenuated replica of the lossless wave signature. Figure 21 shows the relaxation effect due to the second term in the right-hand side of equation (90). This term yields the pulse broadened version of the lossless wave signature and is much smaller in magnitude.

[69] Next, we show, at the same position, a time trace for a Zener solid with coefficients $\tau_\epsilon = \frac{10}{3}$ and $\tau_\sigma = \frac{5}{3}$ (such that $\alpha + \beta = \tau_\sigma^{-1} - \tau_\epsilon^{-1}$). The effect of relaxation due to the first term in the right-hand side of equation (80) is the same as for the Maxwell solid. Figure 22 shows the relaxation effect due to the second term in the right-hand side of equation (80). This term yields the pulse broadened version of the lossless wave signature and is much smaller in magnitude than the attenuated replica but larger than the corresponding contribution for the Maxwell solid.

10. Conclusion

[70] A full time domain solution to the canonical problem of transient elastic *P* and *SV* wave edge diffraction by a

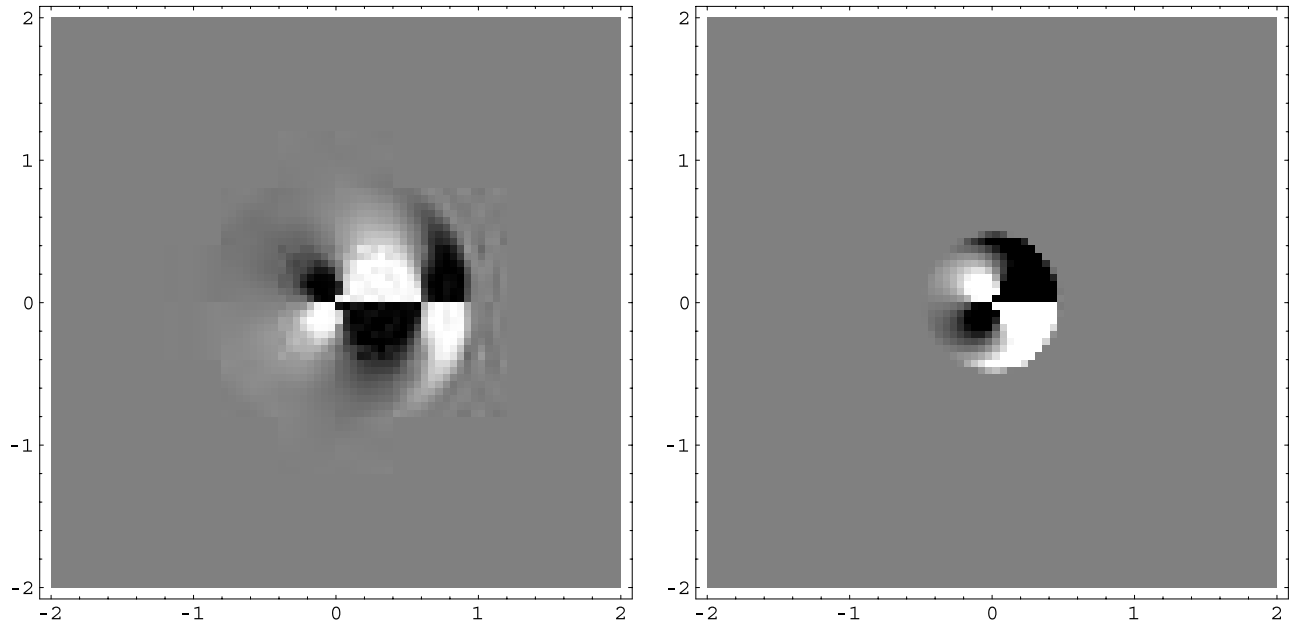

Figure 17. *P*/*SV*, incident *SV*, snapshot of (left) the diffracted *P* wave contribution and (right) the diffracted *SV* wave contribution to v_1; postcritical.

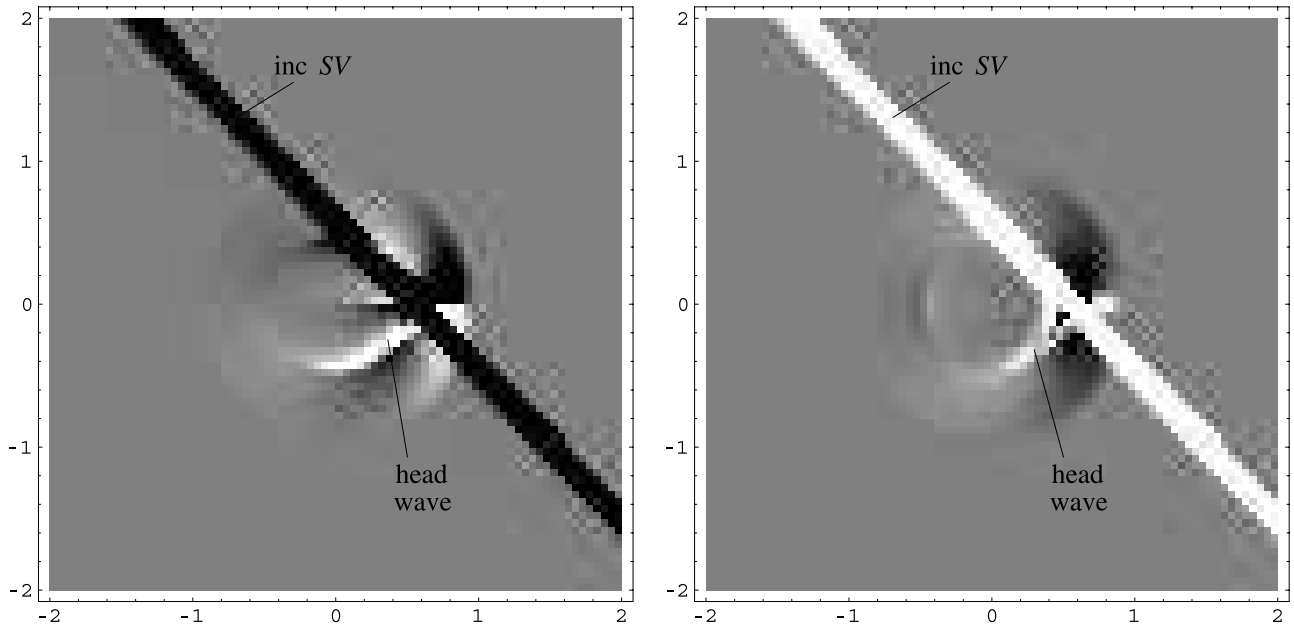

Figure 18. *P*/*SV*, incident *SV*, snapshot of (left) v_1 and (right) v_3; postcritical.

semi-infinite perfect-slip fracture in an isotropic solid has been presented. The case of a lossless hosting solid as well as the cases of a solid with losses of the Zener creep relaxation type and a solid with frictional force and Maxwell relaxation have been considered. The obtained closed-form analytical expressions for the particle velocity components of the wave motion enable one to extract from them quantitative results as to the different features that show up in the physical behavior, all in their dependence on the material parameters of the hosting solid involved.

[71] First of all, the geometrical contributions to the wave field yield the plane *P* and *SV* wave reflection and transmission coefficients pertaining to the partial elastodynamic energy transfer across the fracture. Second, the edge-diffracted cylindrical *P* and *SV* wave contributions yield, apart from showing their exact pulse broadening behavior in space-time, the relevant first-motion diffraction coefficients that are needed in the asymptotic ray theory of elastodynamic diffraction. In addition, the head wave contributions show up. In the expressions for the particle velocity of the wave motion along the fracture, the Rayleigh surface wave contributions are manifest and their excitation coefficients are determined. The marked difference in Rayleigh surface wave contribution to the component of the particle velocity normal to the plane of the fracture versus the one parallel to the plane of the fracture is a straightforward result from the analysis.

[72] In view of their being explicit, the results can prove to be instrumental to a variety of applications in geophysics in all those circumstances where properties of elastic wave motion in the presence of fluid-filled fractures and in a lossless or lossy solid are investigated. As global Earth applications, we mention the problems of characterizing fault zones and detecting the edge of a magma lens. As an application in exploration geophysics, we mention the

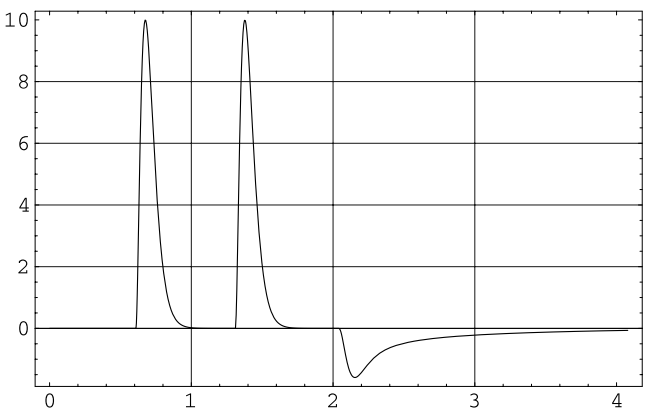

Figure 19. *SH*, time trace (v_2) at $x_1 = 1.0$, $x_3 = -0.2$ (indicated by the small circle in Figure 12; lossless solid.

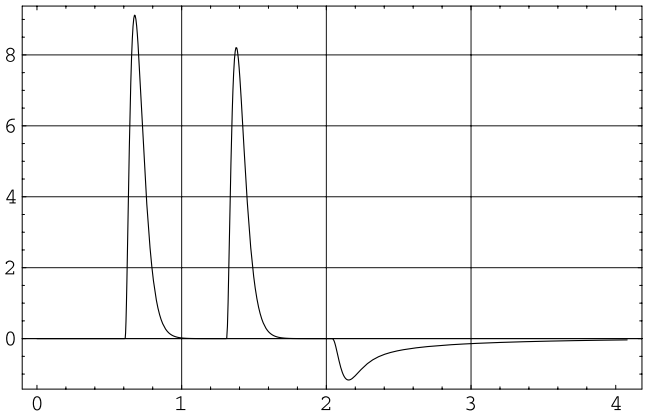

Figure 20. *SH*, time trace (v_2) at $x_1 = 1.0$, $x_3 = -0.2$ of the attenuated constituent; solid with Maxwell relaxation.

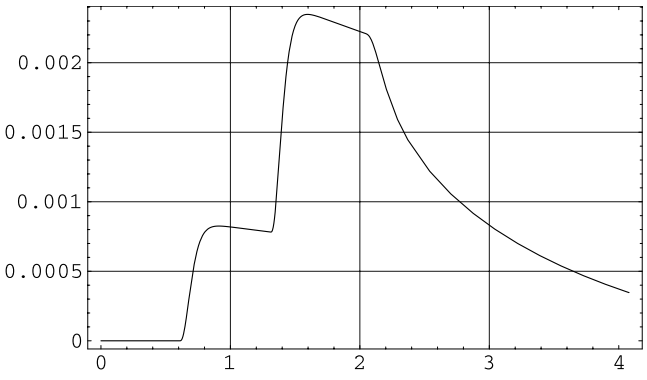

Figure 21. *SH*, time trace (v_2) at $x_1 = 1.0$, $x_3 = -0.2$ of the pulse-broadened constituent; solid with Maxwell relaxation.

evaluation and monitoring of fossil energy reservoirs in the subsurface of the Earth, where a multitude of fluid-filled fractures is present.

Appendix A: Plemelj Additive Decomposition Formulas and Their Application to Wiener-Hopf Kernel Function Factorization

[73] The Plemelj decomposition formulas [*Muskhelishvili*, 1953] deal with the additive decomposition of a function $Q = Q(p)$ of the type

$$Q(p) = Q^-(p) + Q^+(p), \quad p \in \mathcal{L}, \tag{A1}$$

where $\mathcal{L}$ is an oriented curve in the complex p plane with the property that it divides the plane into a domain $\mathcal{D}^-$ to the left of $\mathcal{L}$ and a domain $\mathcal{D}^+$ to the right of $\mathcal{L}$, $Q(p)$ is defined and continuous on $\mathcal{L}$, $Q^-(p)$ is regular in $\mathcal{D}^-$ and $Q^+(p)$ is regular in $\mathcal{D}^+$. For our purposes, $\mathcal{L}$ extends to infinity and is the path of integration in the spectral representation of the wave constituents. It will be shown that under certain additional restrictions the decomposition is accomplished by

$$Q^\mp(p) = \pm\frac{1}{2\pi\mathrm{i}}\int_{\mathcal{L}}\frac{Q(w)}{w-p}\mathrm{d}w, \quad p \in \mathcal{D}^\mp. \tag{A2}$$

A sufficient condition for the right-hand sides of equation (A2) to exist is

$$Q(w) = O(w^{-q}) \quad \text{as } |w| \to \infty \text{ along } \mathcal{L}, \text{ with } q > 0. \tag{A3}$$

Under this condition, Q^- is an analytic function of p that is regular in $\mathcal{D}^-$ and Q^+ is an analytic function of p that is regular in $\mathcal{D}^+$. Now for an arbitrary point $p = p_0$ on $\mathcal{L}$ define

$$Q^\mp(p_0) = \pm\lim_{p\to p_0}\frac{1}{2\pi\mathrm{i}}\int_{\mathcal{L}}\frac{Q(w)}{w-p}\mathrm{d}w, \quad p \in \mathcal{D}^\mp. \tag{A4}$$

A sufficient condition for the limits on the right-hand sides of equation (A4) to exist is that $Q = Q(w)$ satisfies, on $\mathcal{L}$, the Hölder condition

$$|Q(w_1) - Q(w_2)| < A|w_1 - w_2|^\alpha, \quad A > 0, \quad \alpha > 0 \tag{A5}$$

for all $w_1 \in \mathcal{L}$ and $w_2 \in \mathcal{L}$. Under this condition [*Muskhelishvili*, 1953],

$$Q^\mp(p_0) = \frac{1}{2}Q(p_0) \pm \frac{1}{2\pi\mathrm{i}}\mathrm{PV}\int_{\mathcal{L}}\frac{Q(w)}{w-p_0}\mathrm{d}w, \quad p_0 \in \mathcal{L}, \tag{A6}$$

where PV $\int$ denotes the Cauchy principal value of the relevant integral. From this it follows that $Q^-(p_0) + Q^+(p_0) = Q(p_0)$ $p_0 \in \mathcal{L}$.

[74] To apply these results to the kernel factorization problem, we take

$$Q(p) = \log[K(p)], \tag{A7}$$

where $K(p)$ is given by equation (30). Through the way in which we have constructed $K(p)$, in particular its behavior as $|p| \to \infty$, $\log[K(p)]$ satisfies all conditions laid upon $Q(p)$ and hence we can take

$$K^\mp(p) = \exp[Q^\mp(p)], \quad p \in \mathcal{D}^\mp, \tag{A8}$$

with

$$Q^\mp(p) = \pm\frac{1}{2\pi\mathrm{i}}\int_{\mathcal{L}}\frac{\log[K(w)]}{w-p}\mathrm{d}w, \quad p \in \mathcal{D}^\mp. \tag{A9}$$

In view of equation (A6) we have

$$Q^\mp(p_0) = \frac{1}{2}\log[K(p_0)] \pm \frac{1}{2\pi\mathrm{i}}\mathrm{PV}\int_{\mathcal{L}}\frac{\log[K(w)]}{w-p_0}\mathrm{d}w, \quad p_0 \in \mathcal{L}, \tag{A10}$$

from which it follows that

$$K^-(p_0)K^+(p_0) = K(p_0), \quad p_0 \in \mathcal{L}, \tag{A11}$$

as it should be. Since through equation (30) the kernel function $K = K(p)$ is defined everywhere in the complex p plane when cut along the branch cuts $\{p \in \mathcal{C}; 1/c_P < |\mathrm{Re}(p)| < 1/c_S, \mathrm{Im}(p) = 0\}$, the right-hand sides of equation (A9) can be transformed into expressions that are more amenable to numerical evaluation. To this end, the path of integration $\mathcal{L}$ is, in the expression for Q^-, supplemented by a semicircular

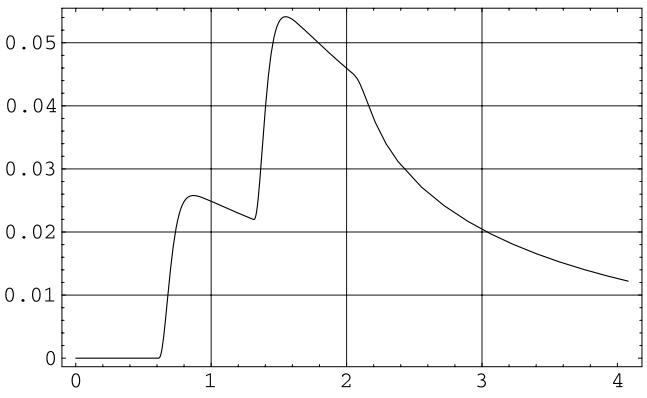

Figure 22. *SH*, time trace (v_2) at $x_1 = 1.0$, $x_3 = -0.2$ of the pulse-broadened constituent; Zener solid.

arc of arbitrarily large radius in $\mathcal{D}^+$ and in the expression for Q^+ by a semicircular arc of arbitrarily large radius in $\mathcal{D}^-$. In view of Jordan's lemma, the contribution from these circular arcs vanishes in the limit as their radius goes to infinity. Subsequently, Cauchy's theorem is applied to the domain in between the resulting closed contours and a loop around the branch cut in $\mathcal{D}^+$ for Q^- and a loop around the branch cut in $\mathcal{D}^-$ for Q^+. Taking into account that along these branch cuts γ_P is imaginary and γ_S is real, we arrive at the following expressions:

$$Q^-(p) = -\frac{1}{\pi}\int_{1/c_P}^{1/c_S} \arctan\left[\frac{w^2\left(w^2 - 1/c_P^2\right)^{1/2}\left(1/c_S^2 - w^2\right)^{1/2}}{\left(w^2 - 1/2c_S^2\right)^2}\right] \cdot \frac{\mathrm{d}w}{w-p}, \qquad \mathrm{Re}(p) < 1/c_P \tag{A12}$$

and

$$Q^+(p) = -\frac{1}{\pi}\int_{1/c_P}^{1/c_S} \arctan\left[\frac{w^2\left(w^2 - 1/c_P^2\right)^{1/2}\left(1/c_S^2 - w^2\right)^{1/2}}{\left(w^2 - 1/2c_S^2\right)^2}\right] \cdot \frac{\mathrm{d}w}{w+p}, \qquad \mathrm{Re}(p) > -1/c_P, \tag{A13}$$

where for the last result a change of the variable of integration into its opposite has been carried out. From the expressions it follows that $Q^-(-p) = Q^+(p)$ for all p.

[75] To circumvent possible difficulties in the numerical evaluation of the right-hand sides of equations (A12) and (A13) due to the occurrence of an algebraic square root behavior near the end points of the integration interval, the variable of integration is replaced by

$$w = \left[\left(1/c_P^2\right)\cos^2(\psi) + \left(1/c_S^2\right)\sin^2(\psi)\right]^{1/2}, \qquad 0 < \psi < \pi/2. \tag{A14}$$

[76] **Acknowledgments.** This work was supported in part by the members of the Consortium Project on Seismic Inverse Methods for Complex Structures at the Center for Wave Phenomena, Colorado School of Mines. The authors wish to thank P. Sonneveld of the Numerical Analysis Group, Delft University of Technology, Netherlands, for his willingness to share with them his expertise in numerics. They also thank R. Madariaga for his many valuable suggestions and comments.

References

Abramowitz, M., and I. A. Stegun, *Handbook of Mathematical Functions*, Dover, Mineola, N. Y., 1965.

Achenbach, J. D., *Wave Propagation in Elastic Solids*, North-Holland, New York, 1973.

Achenbach, J. D., and R. Nuismer, Fracture generated by a dilatational wave, *Int. J. Fract. Mech.*, 77–88, 1971.

Achenbach, J. D., A. K. Gautesen, and H. McMaken, Diffraction of point-source signals by a circular crack, *Bull. Seismol. Soc. Am.*, *68*, 884–905, 1978.

Achenbach, J. D., A. K. Gautesen, and H. McMaken, *Ray Methods for Waves in Elastic Solids*, Pitman, London, 1982.

Aki, K., and M. Fehler, Interpretation of seismic data from hydraulic fracturing experiments at the Fenton hill, New Mexico, hot dry rock geothermal site, *J. Geophys. Res.*, *87*, 936–944, 1982.

Baker, B. B., and E. T. Copson, *The mathematical theory of Huygens' principle*. 2nd ed., pp. 168–177, Clarendon, Oxford, England, 1950.

Carcione, J. M., *Wave Fields in Real Media: Wave Propagation in Anisotropic, Anelastic and Porous Media*, Pergamon, New York, 2001.

Chao, C. C., and J. D. Achenbach, A simple viscoelastic analogy for stress waves, in *Stress Waves in Anelastic Solids*, edited by H. Kolsky and W. Prager, pp. 222–238, Springer-Verlag, New York, 1964.

Coutant, O., Numerical study of the diffraction of elastic waves by fluid-filled cracks, *J. Geophys. Res.*, *94*, 17,805–17,818, 1989.

De Hoop, A. T., *Handbook of Radiation and Scattering of Waves*, Academic, San Diego, Calif., 1995a.

De Hoop, A. T., Similarity analysis of the elastic wave motion in a dissipative solid under a global relaxation law, in *Nonlinear Waves in Solids*, *ASME Book AMR*, vol. 137, edited by J. L. Wegner and F. R. Norwood, pp. 77–82, Int. Union of Theoret. and Appl. Mech., Freiburg, Germany, 1995b.

Fehler, M., and K. Aki, Numerical study of diffraction of plane elastic waves by a finite crack with application to location of a magma lens, *Bull. Seismol. Soc. Am.*, *68*, 573–598, 1978.

Freund, L. B., *Dynamic Fracture Mechanics*, Cambridge Univ. Press, New York, 1998.

Gu, B., R. Suárez-Rivera, K. T. Nihei, and L. R. Myer, Incidence of plane waves upon a fracture, *J. Geophys. Res.*, *101*, 25,337–25,346, 1996.

Kitahara, M., and K. Nakahata, Elastodynamic inversion for shape reconstruction and type classification of flaws, *Wave Motion*, in press, 2003.

Kolsky, H., *Stress Waves in Solids*, Dover, Mineola, N. Y., 1964.

Liu, H.-P., D. L. Anderson, and H. Kanamori, Velocity dispersion due to anelasticity: Implications for seismology and mantle composition, *Geophys. J. R. Astron. Soc.*, *47*, 41–58, 1976.

Mainardi, F., Linear viscoelasticity, in *Acoustic Interactions With Submerged Elastic Structures, Part IV,* edited by A. Guran et al., pp. 97–126, World Sci., River Edge, N. J., 2002.

Muskhelishvili, N. I., *Singular Integral Equations*, 2nd ed., Wolters-Noordhoff, Groningen, Netherlands, 1953.

Noble, B., *Methods Based on the Wiener-Hopf Technique for the Solution of Partial Differential Equations*, Pergamon, New York, 1958.

Pyrak-Nolte, L. J., L. R. Myer, and N. G. W. Cook, Transmission of seismic waves across single natural fractures, *J. Geophysi. Res.*, *95*, 8617–8638, 1990.

Ravichandran, G., and R. J. Clifton, Dynamic fracture under plane wave loading, *Int. J.*, 157–201, 1989.

Sih, G. C., and J. F. Loeber, Wave propagation in an elastic solid with a line discontinuity or finite crack, *Q. Appl. Math.*, *27*, 193–199, 1969.

Sparenberg, J. A., Application of the Hilbert problem to problems of mathematical physics, Ph.D. thesis, Delft Univ. of Technol., Appl. Mech. Lab., Delft, Netherlands, 1958.

Thau, S. A., and T. H. Lu, Transient stress intensity factures for a finite crack in an elastic solid caused by a dilational wave, *Int. J. Solids Struct.*, *7*, 731–750, 1971.

Titchmarsh, E. C., *Introduction to the Theory of Fourier Integrals*, 2nd ed., Clarendon, Oxford, England, 1948.

Titchmarsh, E. C., *The Theory of Functions*, 2nd ed., Oxford Univ. Press, New York, 1950.

Visscher, W. M., Scattering from elastic waves from planar cracks in isotropic media, *J. Acoust. Soc. Am.*, *69*, 50–53, 1981.

Weinstein, L. A., *The Theory of Diffraction and the Factorization Method (Generalized Wiener-Hopf Technique)*, Golem, Boulder, Colo., 1969.

Widder, D. V., *The Laplace Transform*, Princeton Univ. Press, Princeton, N. J., 1946.

Wiener, N., and E. Hopf, Über eine Klasse singulärer Integralgleichungen, *Sitzungsber. Preuss. Akad.*, 696–706, 1931.

Winkler, K. W., Dispersion analysis of velocity and attenuation in Berea sandstone, *J. Geophys. Res.*, *90*, 6793–6800, 1985.

Winkler, K. W., Estimates of velocity dispersion between seismic and ultrasonic frequencies, *Geophysics*, *51*, 183–189, 1986.

A. T. de Hoop and M. V. de Hoop, Center for Wave Phenomena, Colorado School of Mines, Golden, CO 80401-1887, USA. (mdehoop@mines.edu)